Journal of Volcanology and Geothermal Research 435 (2023) 107741

Contents lists available at ScienceDirect

Journal of Volcanology and Geothermal Research

journal homepage: www.journals.elsevier.com/journal-of-volcanology-and-geothermal-research

Dating individual zones in phenocrysts from the 2016–2017 eruption of Bogoslof volcano provides constraints on timescales of magmatic processes

Jamshid Moshrefzadeh [a,*], Pavel Izbekov [a], Matthew Loewen [b], Jessica Larsen [a], Sean Regan [c]

[a] University of Alaska Fairbanks, Alaska Volcano Observatory, Fairbanks, AK, USA
[b] U.S. Geological Survey, Alaska Volcano Observatory, Anchorage, AK, USA
[c] University of Alaska Fairbanks, Department of Geosciences, Fairbanks, AK, USA

ARTICLE INFO

Keywords:
Diffusion chronometry
Magma processes
Mineral chemistry
Crystal growth rate
Clinopyroxene
Bogoslof volcano

ABSTRACT

We investigate the rates of magmatic processes using clinopyroxene diffusion chronometry on volcanic products erupted in August 2017 at the end of the 9-month eruption of Bogoslof volcano. The eruptive products contain plagioclase, clinopyroxene, and amphibole, all of which exhibit sharp chemical boundaries and are occasionally observed in multi-phase crystal clots with shared zoning boundaries across different mineral phases. At the shared boundaries in crystal clots, clinopyroxene and plagioclase continued to grow but abruptly changed composition from Mg# 81.7 ± 5.8 to 72.9 ± 3.0 and $An_{82.5\pm1.4}$ to $An_{61.3\pm5.7}$, respectively. Additionally, the sharp boundary marks where amphibole became unstable and began forming a reaction rim. Synthesizing these observations, we were able to determine that the shared boundaries formed as a result of rapid decompression during magma ascent, followed by storage in a shallow cryptodome, where magma accumulated prior to erupting.

In order to determine the timescales of magma ascent and subsequent crystal residence times, we applied diffusion chronometry on zoned clinopyroxene phenocrysts using Mg# concentrations at 1056 °C determined from Fe—Ti oxide pairs. Our diffusion modeling results show that diffusion began at the stepwise boundaries in clinopyroxenes no more than180 days before the final explosive event.

These results were then used to calculate crystal growth rates for shared plagioclase and amphibole rims, as shared zones in crystal clots indicate that the boundaries in all three phases formed contemporaneously. We calculate growth rates of plagioclase crystals ($1.7 \pm 0.99 \times 10^{-6}$ um/s) and amphibole reaction rims ($2.8 \pm 0.47 \times 10^{-6}$ um/s). The calculated natural growth rate of plagioclase was then used to constrain additional magmatic timescales from growth rate chronometry, results of which support our diffusion timescales.

Our results indicate that the distinct boundaries in all three mineral phases formed due to ascent-driven decompression followed by shallow emplacement of mafic magma that occurred continually throughout the course of the eruption. By subtracting diffusion timescales from the date that the samples were erupted, the oldest crystal boundaries correspond to March 2017, seemingly correlating with increases in both seismicity and SO_2 emissions. These observations may suggest that our petrochronometric results are supported by interdisciplinary observations.

1. Introduction

Phenocrysts in magmas can act as record keepers, providing information about the timing of pressure, temperature, and/or compositional perturbations that occurred prior to and during eruptions. Such changes in magmatic systems can be reflected as chemical gradients recorded in crystal cargo, sometimes creating distinct boundaries between the initial cores and subsequent rims. Diffusivity of chemical compositions across the abrupt compositional boundaries can be used to characterize the timescales of the magmatic processes that triggered their formation (e.g., Dohmen et al., 2002; Costa and Dungan, 2005; Costa et al., 2008; Chakraborty, 2008; Kahl et al., 2011; Kahl et al., 2013; Kilgour et al., 2014; Till et al., 2015; Ruth et al., 2018; Costa et al., 2020). When synthesized with data from other disciplines, results from diffusion chronometry allow us to refine and better characterize the links between petrologic processes and interdisciplinary monitoring data (Kilgour

* Corresponding author.
E-mail address: jamoshrefzadeh@alaska.edu (J. Moshrefzadeh).

https://doi.org/10.1016/j.jvolgeores.2022.107741
Received 27 April 2022; Received in revised form 17 December 2022; Accepted 29 December 2022
Available online 28 January 2023

et al., 2014).

A wide variety of minerals have been utilized in diffusion chronometry studies to constrain magmatic timescales, such as: olivine (Gerlach and Grove, 1982; Martin et al., 2008), clinopyroxene (Morgan et al., 2004), orthopyroxene (Ruth and Costa, 2021; Kilgour et al., 2014), plagioclase (Zellmer et al., 1999; Druitt et al., 2012), sanidine (Till et al., 2015; Charlier et al., 2012), and quartz (Shamloo and Till, 2019; Gualda et al., 2012). When crystal timescales are compared with geophysical and gas monitoring data, retrospective "petrological monitoring" is possible (Saunders et al., 2012a, 2012b). In this case, the petrological and geophysical data from one eruption may be combined to help improve monitoring and forecasting of future eruptions.

The Alaska-Aleutian volcanic arc results from subduction of the Pacific plate beneath the North American plate. Jicha et al. (2006) suggest the age of the onset of subduction and subsequent magmatism in the Aleutians to be approximately 46 Ma, based on $^{40}Ar/^{39}Ar$ age

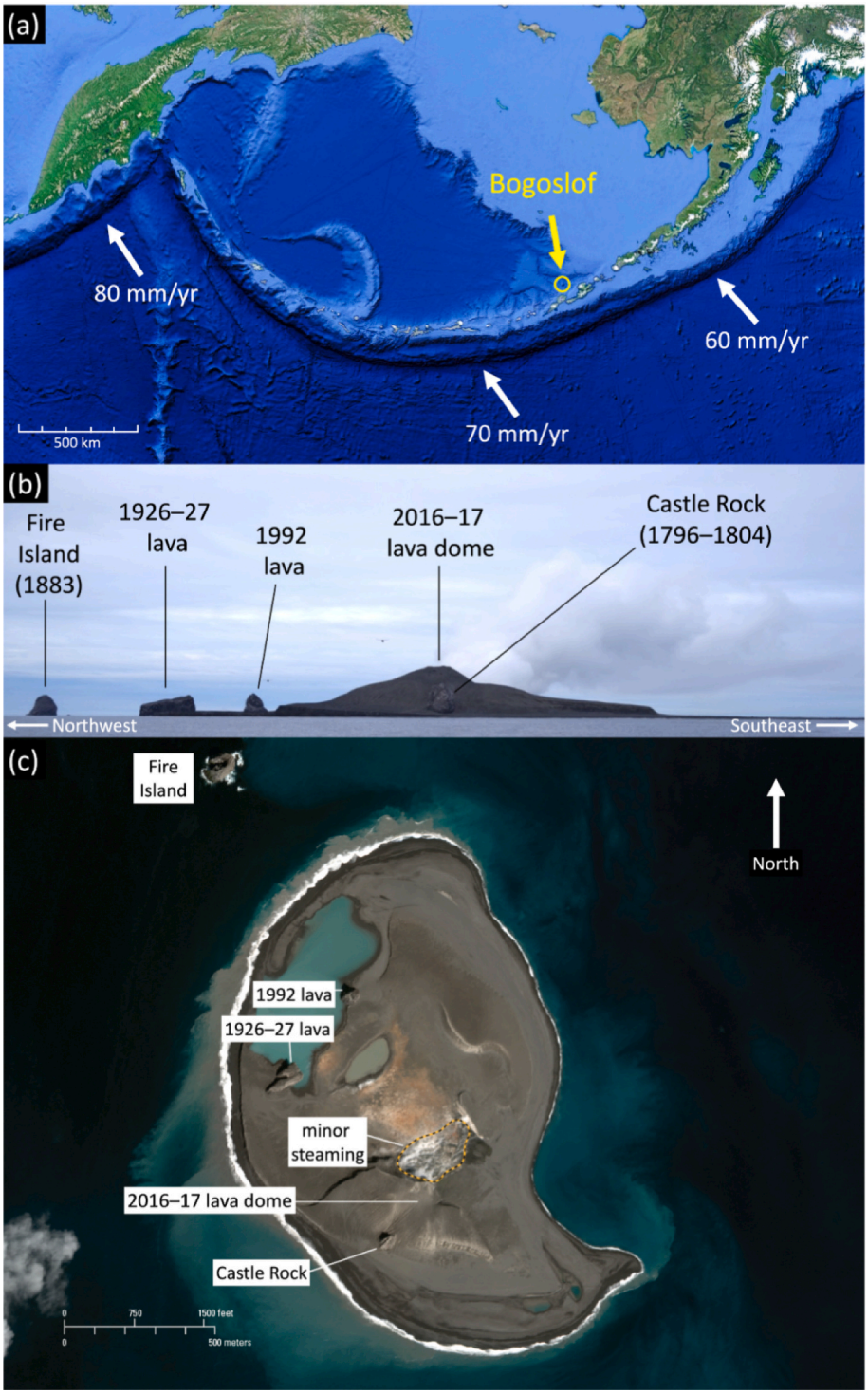

Fig. 1. (a) Google Earth image depicting the location of Bogoslof within the Aleutian Arc. White arrows indicate approximate rate and direction of subduction of the Pacific plate, after Demets et al. (1994). (b) Photograph depicting a northeast-facing view of Bogoslof on July 14, 2019, from Pavel Izbekov. (c) April 20, 2018 WorldView-3 image of Bogoslof, after Chris Waythomas, Alaska Volcano Observatory / U.S. Geological Survey.

determinations coupled with pre-existing K—Ar ages. Extending to the west from the Gulf of Alaska, the Alaska-Aleutian Arc intersects with the Kamchatka-Kuril Arc, which continues southward for approximately another 2000 km. This complex is also connected to neighboring areas of subduction, such as the Japan, Izu-Bonin, and Mariana trenches (Ruppert et al., 2007).

Subduction rate varies along the Aleutian Arc. The slowest rate (about 60 mm/yr) occurs in the eastern portion, then increases by about 10 mm/yr for the central portion, and then again for the very western zone of the arc, where the Pacific plate subducts beneath Kamchatka at around 80–90 mm/yr (Fig. 1a) (Demets et al., 1994; Ruppert et al., 2007; Scholl and von Huene, 2007). The transition to transform plate movement in the far western Aleutian ridge creates a complex shear zone which significantly decreases the abundance of volcanoes between Bowers ridge and the Kamchatka peninsula (Scholl, 2007).

Along the Alaskan portion of the Aleutian Arc, there are >130 volcanoes and volcanic fields which have been active within the last two million years. Of these volcanic features, about 90 have been active within the Holocene, and over 50 since the 18th century (www.avo.alaska.edu). Generally, the area of greatest magmatic output within the Aleutian Arc is thought to be the center of the arc. This is supported both by volume of volcanoes and by the frequency of eruptions (Fournelle et al., 1994).

The mid December 2016 to late August 2017 eruption of Bogoslof Island, Alaska, (Bogoslof; Bogoslof volcano) presents an opportunity to use crystal compositions, textures, and the diffusion chronometry technique to examine the pre and *syn*-eruptive timescales of magmatic processes. Bogoslof is a predominantly submarine stratovolcano with low elevation above sea level, and is located approximately 50 km behind the main volcanic front of the Aleutian Islands (Fig. 1a). Bogoslof possesses two main subaerial landmarks: Bogoslof Island and Fire Island (Fig. 1b and c). The authors acknowledge that Bogoslof Island is known by multiple Indigenous names: Agashagok, Agasaagux, and Tanaxsidaagux (Marsh and Leitz, 1979; Miller et al., 1998; Waythomas and Cameron, 2018). For the context of this work, the volcano will be referred to as Bogoslof, but we express our deepest respect and gratitude for our Indigenous neighbors.

Bogoslof eruptions are typically characterized by the effusion of basalt to basaltic andesite lava domes along with explosive eruptions generated by water-magma interactions that result in the formation of tuff rings, and eruption clouds that are broadly ash-poor, with fallout present predominantly within 100 km of the vent (Waythomas et al., 2020). The most recent eruption of Bogoslof began on December 12, 2016, and continued until August 30, 2017 (Waythomas and Cameron, 2018). The vent was submerged during the majority of the 2016–2017 eruption, resulting in seawater playing a significant role in eruption dynamics (Fee et al., 2019). There were, however, several longer-lasting events that led to the formation of lava domes, thereby allowing the vent to shift above sea level and produce plumes that were more ash-rich (Fee et al., 2019; Schneider et al., 2020). At least 70 explosive events occurred during the eruption, as well as two dome-building periods (Coombs et al., 2018; Coombs et al., 2019; Tepp et al., 2019; Van Eaton et al., 2020). Although there is no seismic network on the remote Bogoslof, the Alaska Volcano Observatory monitored the eruption using seismic stations on neighboring Umnak and Unalaska Islands, a regional infrasound network, and satellite data providing visual and gas geochemistry data. Coombs et al. (2019) provide a distinction of two main phases to describe the eruption: phase one, which took place from December 12, 2016 through March 13, 2017, and phase two, from May 17, 2017 to August 30, 2017. The two phases are separated by a 65-day-long eruptive hiatus. The final events of the eruption (August 27–282,017) consisted predominantly of short explosions (<6 min), with the exception of the final event on August 30, 2017, which lasted almost an hour (Coombs et al., 2019).

This study builds on the work of Loewen et al. (2019), which provides a comprehensive overview of the geochemistry and petrology of the 2016–2017 Bogoslof eruptive products. Here we add new information about the mechanics and timescales of magma replenishment and discuss evidence for the fusing and recycling of trachytic magma. We use the timescales determined from diffusion chronometry applied to the multi-phase crystal clots to calculate the rates of plagioclase rim growth and amphibole reaction rim formation. Our results indicate that the stepwise boundaries in crystalline phases of the magmas erupted by Bogoslof in August 2017 initially formed due to decompression during the ascent of mafic magma which was subsequently emplaced in a shallow storage area (Loewen et al., 2019; Waythomas et al., 2020). The range in diffusion timescales indicates that the shallow cryptodome storage area experienced continuous magma replenishment throughout the course of the eruption, with varying diffusion timescales recording the individual residence times of crystals. Activity at Bogoslof during the times indicated by diffusion results is additionally characterized by increased seismicity and SO_2 rates, suggesting that our results are consistent with multiple interdisciplinary observations.

2. Methodology

2.1. Samples

This study focuses on 17 petrographic thin sections, which include 11 samples of basaltic scoria, 5 trachyandesitic dome fragments, 2 trachyte pumices, and 3 mafic enclaves.

Compositional transects for diffusion modeling were measured on clinopyroxene phenocrysts from 8 petrographic thin sections: 6 of basaltic composition which erupted on August 30, 2017, and 2 trachyandesites which uplifted between mid-December 2016 and July 2017 (Waythomas et al., 2020). Additional descriptions of these samples, including sample metadata, whole rock and glass geochemistry, are available in Loewen et al. (2019) and with this paper in the electronic supplementary material.

2.2. Analytical methods

We used the JEOL JXA8530F electron probe micro-analyzer (EPMA) hosted at the University of Alaska Fairbanks Advanced Instrumentation Laboratory to conduct quantitative analyses of mineral phases. This EPMA is automated with Probe for EPMA software (Donovan et al., 2011). We used a 15 keV, 10 nA, and 10 mm working distance focused beam for analyses of all mineral phases. High-resolution backscattered electron (BSE) images were acquired using the same analytical conditions. Initial mineral analyses of the erupted products of the 2016–2017 eruption of Bogoslof are described by Loewen et al. (2019). In this paper, we will briefly summarize and subsequently build upon their results. We add analyses of detailed core-rim transects across clinopyroxene, plagioclase, and amphibole phenocrysts, as well as analyses of phases hosted in amphibole reaction rims. To obtain minor element concentrations in plagioclase, secondary analyses that specifically targeted stark chemical boundaries were set to 20 keV and 40 nA. Please refer to the Electronic Appendix for counting times, assigned calibration standards, and analytical uncertainties.

The primary criteria considered when targeting clinopyroxene phenocrysts for diffusion analyses is the apparent presence of a sharp boundary between the crystal core and rim. This boundary may be observed in samples under petrographic microscopes, but is most readily seen in back scattered electron imagery, where the greyscale of images serves as an indicator of chemical composition. We targeted crystals that possess either euhedral or subhedral core-rim boundaries. The euhedral boundaries are associated with normal zoning: decreasing Mg# from core to rim, whereas subhedral boundaries exhibit reverse zoning, with rims of higher Mg# relative to cores.

EPMA transects were taken across the distinct core-rim boundaries of crystals with 2 μm increments between each analyzed point. Each targeted crystal was analyzed with 2–5 core-to-rim transects in order to

select the most favorable profile from each crystal. We performed Monte Carlo simulations to account for the beam interaction with the targeted crystal (Drouin et al., 2007). The three-dimensional nature of the EPMA analyses indicates that curvature of measured profiles may be artificially smoothened or straightened, depending on the orientation of crystallographic axes relative to the way the crystal has been cut during sample manufacturing. Monte Carlo simulations aided in determining the most accurate profile from the 2–5 transects per phenocryst by accounting for these potential artificial changes in measured profiles.

When determining the most desirable profile, we additionally considered selected the goodness of fit of our model paired with calibrated grayscale transects acquired from annotated BSE images of analyzed phenocrysts showing the precise locations of EPMA analyses from the open-source software ImageJ in order to compare calibrated profile values to the transects of measured EPMA data (Abramoff, 2007; Saunders et al., 2012a; Ruth et al., 2016). This comparison is helpful in determining obliquity of the boundary. If the EPMA transect produces a profile that is significantly more curved or off-set relative to the profile from the calibrated BSE image, this can be interpreted as evidence suggesting the boundary between core and rim is not perpendicular to the cut of the crystal. This could result in an artificial curve in the EPMA profile, due to the three-dimensional nature of the electron beam interaction. Due to their high resolution and two-dimensional nature, it is likely that calibrated BSE profiles will always result in steeper profiles relative to EPMA transects, but comparing the two can aid in the process of selecting the most desirable EPMA transect.

While calibrated grayscale values may theoretically be used for diffusion modeling, the short distance between measured EPMA points made grayscale calibration on larger phenocrysts difficult. It is for this reason that we use the calibrated grayscale transects only to better determine the relative shape of the profiles to our diffusion modeling results, while using the Mg# values from EPMA analyses directly for the modeling. All BSE images of clinopyroxene used for diffusion modeling, along with the corresponding conditions of the images, are included in the electronic supplementary material.

2.3. Diffusion modeling

One drawback of thin section manufacturing and the analysis of in situ crystals is that phenocrysts are rarely cut precisely along the a-, b-, or c- axes. The results of Schwandt et al. (1998) indicate that diffusion in pyroxene occurs most rapidly along the c- axis. We targeted diffusion gradients which appeared to be perpendicular to the c-axis of exposed crystals by aspect ratio, in order to measure diffusion across the shorter a- or b- axes. This means that our diffusion modeling results would provide a more representative timescale, whereas diffusion along the c-axis often results in erroneous underestimates due to the rapid diffusion along this axis (Costa and Dungan, 2005; Allan et al., 2013; Dohmen et al., 2017). A similar technique was applied by Allan et al. (2013) for orthopyroxene diffusion studies, where rim growth was observed to be considerably faster parallel to the c- axis, hence only profiles approximately parallel to the a- or b- axis were considered (Dohmen et al., 2017). We additionally verified that the modeled gradients were the sharpest observed compositional boundary.

Diffusion coefficients can be determined based on a single Arrhenius relation:

$$D = D_0\, exp\,(-Q/RT) \tag{1}$$

where D is the diffusion coefficient, D_0 is a pre-exponential factor, Q is the activation energy, R is the universal gas constant, and T is the absolute temperature. To determine the diffusion coefficient for Fe—Mg interdiffusion in clinopyroxene used in this study, we use the following equation from Müller et al. (2013) where D_0 and Q have been determined experimentally along the c-axis of clinopyroxenes:

$$D^{Fe\text{–}Mg} = 2.77 \pm 4.27 \times 10^{-7} exp\,(-320.7 \pm 16.0\ kJ/mol/RT)\ m^2/s \tag{2}$$

Analogous results for D_0 and Q values are shown by Dimanov and Wiedenbeck (2006), with the exception of a slightly lower activation energy (297 kJ/mol). This difference, however, is negligible when we consider the uncertainty provided by Müller et al. (2013).

Results of Müller et al. (2013) indicate that there is no detectable dependence of $D^{Fe\text{–}Mg}$ on clinopyroxene composition over a range of 800–1200 °C and Fe/Mg ratio between Di_{93}–Di_{65} used in their experiments. These results overlap with and are comparable to the temperatures and composition used in this study. Dimanov and Wiedenbeck (2006) note that there may be a dependence on fO_2 relating to aluminum content of experimental clinopyroxene, which then required a Fe^{3+} substitution for charge balance. The substitution of Fe^{3+} subsequently affected the diffusion coefficient. Although this is noteworthy, further experimental studies on pyroxene crystals with overlapping Fe contents and a range of Al contents are necessary to quantify the dependence of $D^{Fe\text{–}Mg}$ on Al (Müller et al., 2013).

The modeled composition of diffusion from core to rim across a stepwise boundary can be calculated using eq. 3, after Philpotts and Ague (2009):

$$C(x,t) - C_1 = \frac{(C_0 - C_1)}{2}\, erfc\left(\frac{x}{2\sqrt{Dt}}\right) \tag{3}$$

where C_0 and C_1 represent the two different compositional plateaus, x is relative distance (μm), D is the diffusion coefficient determined from eq. 2, and t is time. In addition to the center of each profile, the values of C_0, C_1, and time (age of the diffusion boundary, days) are determined numerically using the algorithm of Lasdon et al. (1974), implemented in the Solver routine of the 2016 Microsoft Excel software.

Diffusion is highly dependent on temperature. We used the temperature of 1056 °C ± 20 °C to model diffusion, based on Fe—Ti oxide thermometry results of Loewen et al. (2019). The uncertainty of our age calculations is determined by applying the diffusion model at three different temperatures, based on the potential error based on the uncertainties of the magnetite-ilmenite geothermometer described by Ghiorso and Evans (2008). Higher temperatures initiate faster diffusion, resulting in younger timescales. The opposite is true for lower temperature modeling. By propagating the thermal uncertainty of ±20 °C in our diffusion models, we may assume that the system is at a constant temperature while accounting for the possible range in temperatures with the included error bars.

3. Results

3.1. Overview of eruptive products

The magmas produced by the 2016–2017 eruption of Bogoslof are diverse, including basaltic scoria, trachyandesite dome lava, and trachyte pumice. Basaltic scoria dominates the erupted material found on the island surface. Trachyandesites are more evolved than the basaltic scoria, and were thought to have been erupted primarily as an uplifted cryptodome at the early phase of the eruption in December 2016, with minor fragments incorporated into subsequent explosive events (Loewen et al., 2019; Waythomas et al., 2020). Both the basaltic scoria and the trachyandesite contain a primarily plagioclase-amphibole-clinopyroxene mineral assemblage, while the trachyte contains plagioclase, clinopyroxene, and relic amphibole structures, along with biotite, sanidine, quartz, and titanite (Loewen et al., 2019). Clinopyroxene is abundant in the basalt, with many phenocrysts exhibiting distinct compositional boundaries between the cores and rims. Multiphase crystal clots show simultaneous growth of compositionally distinct rims in plagioclase and clinopyroxene that appear to have formed at the same time as reaction rims in the amphiboles. Pairs of Fe—Ti oxides found in the trachyte provide estimates of temperature

and oxygen fugacity, which are critical for accurate petrological modeling of the pre and *syn*-eruptive processes (Loewen et al., 2019).

3.2. Phenocryst compositions and textures by lithology

Phenocrysts within the 2016–2017 erupted products frequently have outer rims separated from predominantly homogeneous and clean crystal cores by sharp compositional boundaries. Across the three lithologies, these distinct boundaries are present in plagioclase, clinopyroxene, and amphibole. Plagioclase is present in all three erupted lithologies, while the distinctly zoned clinopyroxenes and amphiboles are found only in the basalt and trachyandesite. Representative BSE images of zoned mineral phases are provided in Fig. 2. Compositional ranges of the phenocryst assemblage are shown in Figs. 3 and 4. Variance in crystal compositions are presented as means, plus or minus one standard deviation. We will briefly describe the chemical boundaries present in the trachyandesite and trachyte, but focus primarily on those exhibited within phenocrysts hosted in basalt, as it was the most abundant lithology erupted.

3.2.1. Basalt

Plagioclase compositions in the basalt range from $An_{41.2}$ to $An_{92.6}$ and plagioclase occurs as phenocrysts (>500 μm), microphenocrysts (50–500 μm), and microlites (<50 μm). Typical plagioclase core compositions are $An_{82.5\pm1.4}$, with fine oscillatory zonation. Cores occasionally exhibit a dip in anorthite content from $An_{82.5}$ to $An_{77.4}$ as they

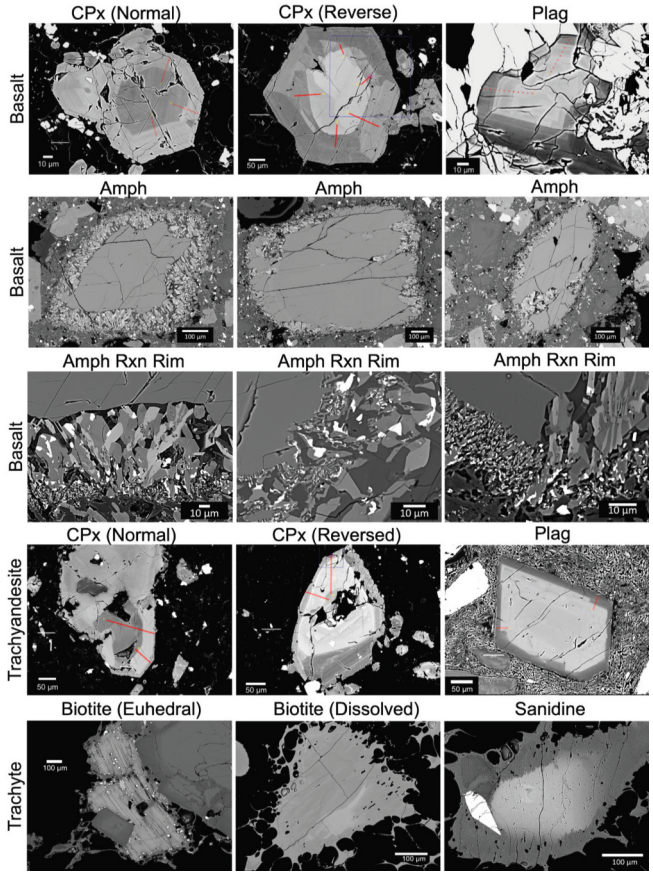

Fig. 2. Back-scattered electron images of phenocrysts from the eruptive products of Bogoslof. Row 1 shows both normally and reversely zoned boundaries in clinopyroxene (CPx), and zones in plagioclase (Plag) in basalt. Rows 2 and 3 show the variety of reaction rim (Rxn Rim) widths on amphiboles (Amph), along with microstructures in reaction rims. Row 4 displays both normally and reversely zoned boundaries in clinopyroxene, and sharp boundaries in Plag in trachyandesite. The bottom row shows minor phases found in trachyte pumice.

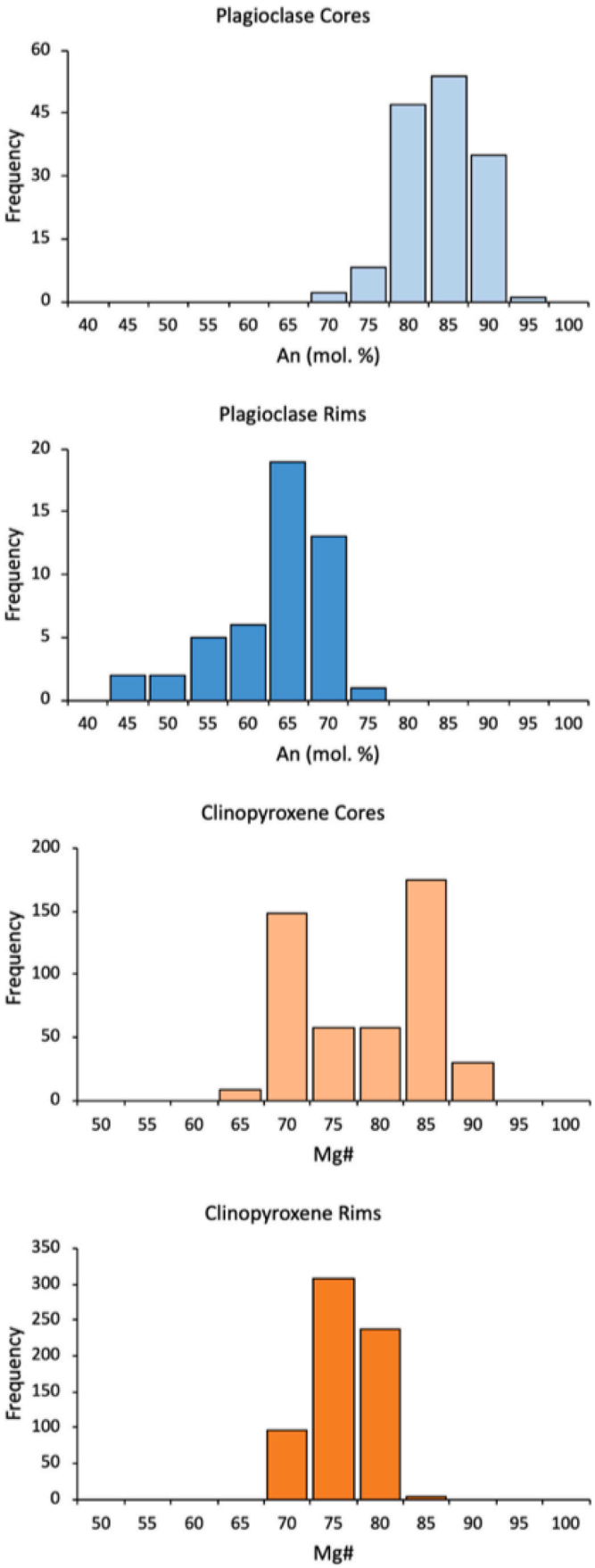

Fig. 3. Histograms depicting the compositional ranges of plagioclase and clinopyroxene cores and rims from samples of basaltic scoria.

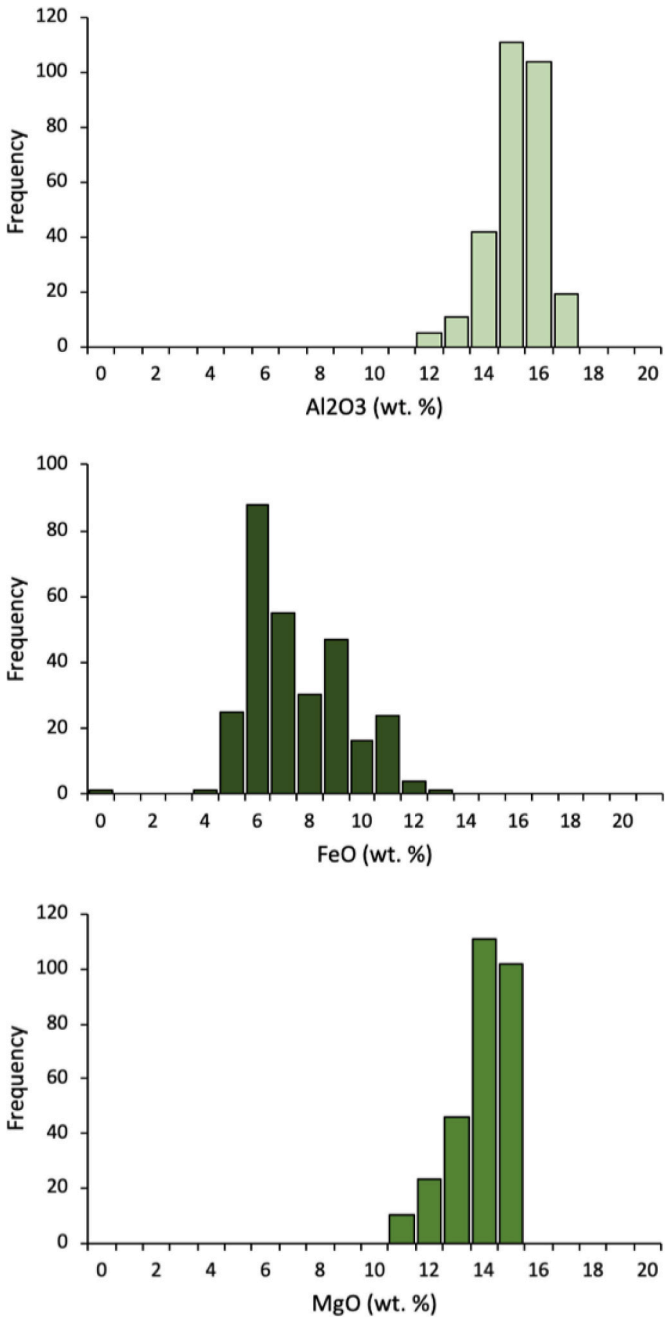

Fig. 4. Histograms depicting the range of elemental compositions of amphibole phenocrysts in samples of basaltic scoria.

approach the core to rim boundary, until abruptly dropping to $An_{61.3\pm5.7}$ in the normally zoned rims. Loewen et al. (2019) note the presence of plagioclase phenocrysts which exhibit anhedral, sometimes sieved ~An_{82} core, followed by a dissolution boundary marking an increase to about An_{90}. Such crystals also exhibit sharp boundaries separating the inner crystal from the lower anorthite rims. Interestingly, despite the presence of these plagioclase crystals which exhibit reverse zoning between their anhedral cores and calcic mantles, we do not see any plagioclase which exhibit reverse zoning between cores and final rims (Fig. 3).

Clinopyroxene phenocrysts, microphenocrysts and microlites are euhedral with magnesium numbers (Mg#) that range from 61.3 to 88.7 (Fig. 3). We calculate Mg# as molar Mg/(Mg + Fe) where all Fe is treated as Fe^{2+} (following Ruth and Costa, 2021). We observe both normally and reversely zoned clinopyroxene phenocrysts within basalts (Fig. 2). Normally zoned crystals exhibit a core with Mg# = 81.7 ± 5.8 that is followed by a euhedral boundary and a subtly oscillatory zoned rim with an average Mg# = 72.9 ± 3.0. Reversely zoned clinopyroxenes exhibit a homogeneous core with a significantly lower Mg# = 69.0 ± 2.1. The cores are predominantly subhedral to anhedral, surrounded by a dissolution boundary that separates them from their distinct rims. Rims are characterized by a higher Mg# = 75.5 ± 2.4 and often exhibit sector zoning (Hollister and Hargraves, 1970).

In basalts, amphiboles occur as phenocrysts which are predominantly magnesio-hastingsite in composition (Leake, 1978). Fig. 4 shows the compositional range of major elements of amphibole phenocrysts from basalt samples. Further classification of all analyzed amphiboles is provided in the electronic supplementary material. The cores of amphiboles are characterized by 11.13–14.65 wt% MgO and 9.95–15.09 wt % FeO(t), while their rims range from 12.84 to 14.25 wt% MgO and 9.45–11.87 wt% FeO(t). The compositionally sharp boundaries separating cores and contrasting rims are seemingly less abundant in amphiboles than within the clinopyroxene and plagioclase.

Amphibole phenocrysts are regularly surrounded by 10–100 um wide reaction rims. Within amphibole reaction rims, the microlite mineral assemblage comprises clinopyroxene, orthopyroxene, plagioclase, and Fe—Ti oxides. Approximate modal percentages suggest that clinopyroxene and orthopyroxene are the most abundant phases, ranging within 25–35% and 28–30%, respectively. Plagioclase ranges 12–24%, whereas the abundance of Fe—Ti oxides is <20%. Clinopyroxene microlites in amphibole reaction rims range from 68.5 to 73.7 Mg#, with an average of 70.3 Mg#. Orthopyroxene microlites have a broader range of 54.8–70.9 Mg#, averaging Mg# 63.9. Composition of plagioclase microlites varies in the range of 37.8–51.9 mol% anorthite, and has an average of $An_{45.2}$.

3.2.2. Trachyandesite

Within the trachyandesites, plagioclase with noticeable core-rim boundaries exhibit normal zoning: $An_{80.4\pm2.4}$ cores that drop to a rim composition of $An_{59.6\pm5.6}$. The composition of the calcic cores overlaps with those of the basalt-hosted plagioclase, while the plagioclase rims in the trachyandesites trend slightly more sodic than basaltic plagioclase rims, remaining consistent with a more evolved bulk rock composition (Loewen et al., 2019).

Sharp chemical boundaries in clinopyroxenes hosted in the trachyandesite are similar to those hosted in basalt with two broad zoning populations. Phenocrysts within the first population are normally zoned and with a core of Mg# 73.6 ± 2.5 that transitions abruptly to a weakly oscillatory zoned rim with an average Mg# 67.5 ± 2.3. The second population of clinopyroxene in trachyandesite exhibit an opposite pattern; characterized by reverse compositional zoning and a texturally heterogeneous Mg# 63.2 ± 0.8 core that is often patchy and subhedral, followed by a subtle oscillatory zoned rim of Mg# 68.5 ± 1.3.

Amphiboles in the trachyandesites are compositionally heterogeneous. Phenocryst cores have 10.94–13.12 wt% MgO and 11.45–14.69 wt% FeO(t), and rims 9.93–10.36 wt% MgO and 14.96–16.55 wt% FeO (t), separated by a euhedral to subhedral core-rim boundary. Amphiboles within this lithology occur both with and without reaction rims.

3.2.3. Trachyte pumice

Plagioclase phenocrysts exhibiting sharp boundaries within the trachyte pumice exhibit sharp normal zoning, with euhedral $An_{83.1–89.6}$ cores that change abruptly to oscillatory-zoned $An_{30.4–35.7}$ rims. The composition of these rims overlaps with the overall composition and zoning pattern found in the other population of trachyte-hosted plagioclase that lack a core-rim boundary. In addition to plagioclase, phenocrysts and microlites of sanidine are also present in trachyte. The sanidine microlite compositions are 58.2 ± 1 mol% orthoclase.

Unlike plagioclase, clinopyroxenes within the trachyte pumice possess relatively constant composition of Mg# = 69.8 ± 2.3. The composition of clinopyroxene in trachyte matches the rim compositions

of the clinopyroxenes found in trachyandesite (Mg# = 68.5 ± 1.3) (Loewen et al., 2019).

Fe—Ti oxides in the trachyte pumice include ilmenite and titanomagnetite. Loewen et al. (2019) measured the composition of six magnetite-ilmenite pairs as 0.25–0.27 ulvospinel and 0.72–0.75 magnetite for titanomagnetite, and 0.57–0.63 ulvospinel and 0.37–0.43 magnetite for ilmenite (Fig. 5).

3.3. Fe—Ti Oxide and two feldspar thermometry

Temperature has a first-order control on the rate of chemical diffusion, and we do not directly know the temperature of the dominant basaltic lithology of erupted samples. Although there are multiple methods that we may apply to attempt to constrain the temperature of the basalt, abundant ilmenite-magnetite pairs are found in the trachyte pumice which erupted both alongside the basalt and as preserved inclusions within the basalt. These ilmenite-magnetite pairs occur as microlites (<50 μm). The pairs pass the Mn/Mg equilibrium test of Bacon and Hirschmann (1988), thus we can apply the revised ilmenite-magnetite geothermometer of Ghiorso and Evans (2008). We found that the pre-eruptive temperature and oxygen fugacity of trachyte pumices range from 977 to 1056 °C and NNO + 1.27 to NNO + 1.65 respectively (Loewen et al., 2019; Fig. 5).

Although the trachyte pumice made up <5% of surface cover during the island visit in 2018, it remains a crucial constituent in understanding the processes that lead to the most recent eruption. The pumices are highly vesicular and have a microlite-free glassy groundmass, but on a vesicle-free basis are 90% crystalline. Trachyte samples show a eutectic assemblage of sanidine, plagioclase, clinopyroxene and quartz, low temperature accessory minerals such as titanite and biotite, and include relict amphibole pseudomorphs. A number of hand samples of the trachyte pumice exhibit macroscopic evidence of magma mixing and reheating, such as pumice coated in a mafic rind and samples of physically mingled pumice and basaltic components (Fig. 6a). Trachyte pumice hand samples additionally exhibit textural evidence for recharge-induced remelting; there are observable small (2–8 mm) inclusions in the pumice, usually found suspended by glassy strands of trachyte in the center of a vesicle significantly larger than those found in the overall groundmass of the trachyte (Fig. 6b). These inclusions are dense and angular, suggesting that they are lithics which were incorporated into the host magma in a solid state and did not re-melt due to a higher melting point of the lithic inclusions. The glassy strands and larger vesicles surrounding the lithic inclusions likely formed due to the preferred nucleation of vesicles on the surface of inclusion. This phenomenon is known as heterogeneous nucleation and it has been documented for magnetites (Gardner and Denis, 2004). These observations all suggest that the trachyte magma was a near-solidus resident magma that was rejuvenated by the dominant basalt lithology during the 2016–2017 eruption.

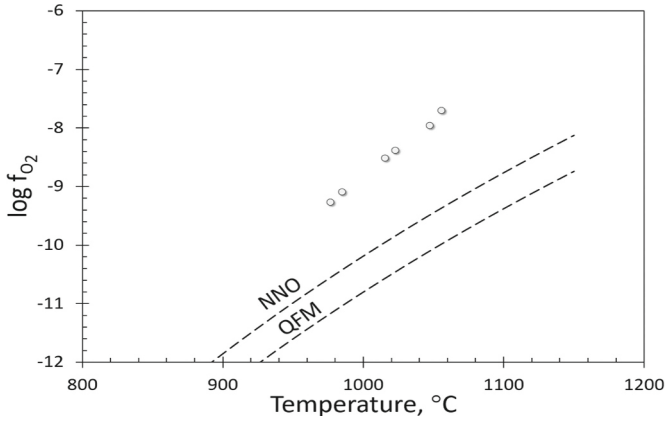

Fig. 5. Results from Loewen et al. (2019) showing the pre-eruptive temperature and oxygen fugacity of trachyte pumice based on the revised calibration of the ilmenite–magnetite geothermometer by Ghiorso and Evans (2008). The pre-eruptive temperature and oxygen fugacity range from 977 to 1056 °C and from NNO + 1.27 to NNO + 1.65, respectively. Circles represent data points from 6 mineral pairs from trachyte pumice, compared to the modeled dashed lines showing NNO and QFM buffers.

Ilmenite-magnetite pairs rapidly equilibrate at magmatic temperature, even recording cooling timescales of extruded lava flows (e.g., Venezky and Rutherford, 1999). Thus, this thermometer can reliably record eruption temperatures in rapidly quenched lavas but has a short memory for earlier pre-eruptive magmatic conditions. We suggest that the upper 1056 °C temperature of ilmenite-magnetite pairs in 2016–2017 trachyte records equilibration with the temperature of the rejuvenating host, and thus provides at least a lower bound constraint on the basalt temperature for diffusion modeling.

The two-feldspar thermometer of Putirka (2008) provides an alternative method to estimate the temperature of the trachyte. Using measured sanidine and plagioclase microlite compositions we calculate a temperature of approximately 870 °C assuming shallow storage conditions (i.e. < 3 kbar). Given that the two-feldspar thermometer re-equilibrates slower than that of Fe—Ti oxides, we interpret the feldspar thermometer results to capture a range of temperatures spanning between the original cold temperature of the resident trachyte and the contrastingly hot temperature of the juvenile basalt from the most recent eruption.

Compositional similarity to the 1796–1804 Castle Rock eruption suggests that the 2016–2017 trachyte could be a residual magma from the old eruption (Loewen et al., 2019). An analogous process occurred during the 2018 eruption of Kilauea Volcano, where the first and only observed eruption of andesite lava in Hawaii was inferred to be the result of an isolated pocket of fractionated and highly crystalline siliceous magma being brought to the surface by the down-rift propagation of fresh mafic magma (Gansecki et al., 2019).

3.4. Diffusion modeling results

One profile was selected from the 2–5 profiles measured on each clinopyroxene phenocryst; Fig. 7 shows an example of our measurements. By applying eq. 3, where $T = 1056$ °C, we calculated a diffusion coefficient (logD) for Fe—Mg interdiffusion in clinopyroxene of −15.17 cm^2/s. Our diffusion modeling results show that distinct compositional boundaries in Bogoslof clinopyroxenes are <180 days old (Table 1; Fig. 8). By subtracting our resulting timescales from the day the samples were erupted, the oldest diffusion timescales correspond to March 2017 (Fig. 8; Fig. 9). The process of diffusional relaxation is driven by the chemical gradient between crystal zones. The smoothening of the initially stepwise profiles thereby records the date of formation of each boundary (Fig. 10). Diffusion timescales from normally and reversely zoned clinopyroxene phenocrysts overlap, suggesting that the processes that formed the final rims occurred nearly simultaneously, regardless of chemical zonation (Table 1). Additionally, assuming a similar modeling temperature, diffusion timescales from crystals hosted in trachyandesite are similarly short (Table 1). Evidence described in Loewen et al. (2019) shows that the trachyandesite was not a juvenile lava of the 2016–2017 eruption. Because of this, the resulting timescales from diffusion modeling in trachyandesite-hosted phenocrysts are not included in the temporally synthesized interdisciplinary monitoring data (Fig. 10).

3.5. Multi-phase crystal clots and growth rates

The preservation of similar chemical changes recorded within the core-rim boundaries across multiple phases in crystal clots indicates that the distinct boundaries within all three mineral phases (clinopyroxene, plagioclase, and amphibole) formed contemporaneously. An analogous observation of an olivine grain reacting to form a rim of orthopyroxene

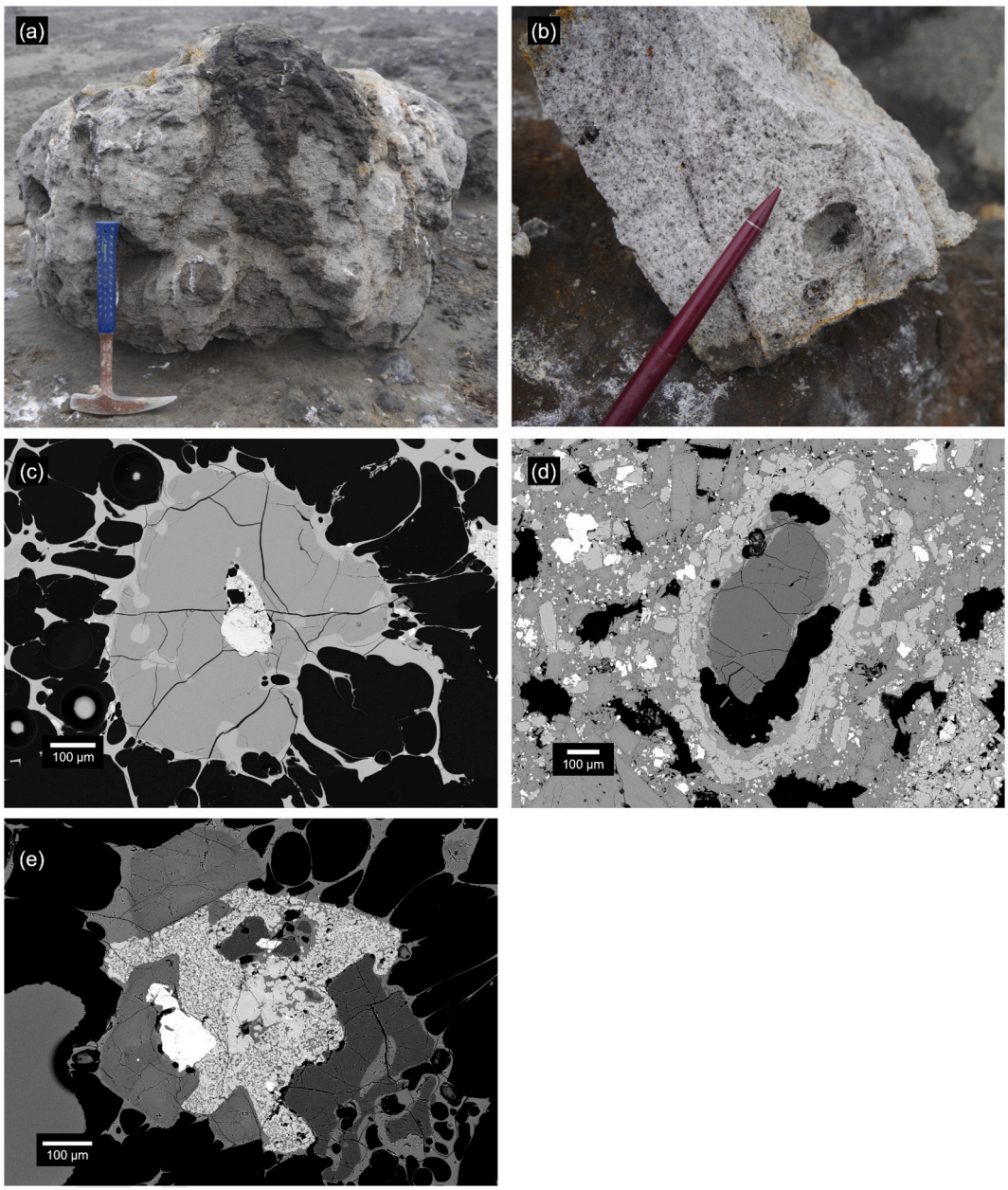

Fig. 6. Images of 2017 eruptive products that exhibit macroscopic (a-b) and microscopic (c-e) evidence of fusing and recycling of trachytic material by basaltic magma. (a) Photograph of trachyte bomb mingled with dark basaltic scoria. (b) Photograph of trachyte pumice sample with small (2–8 mm) mafic inclusions suspended by glassy strands of trachyte in the center of a distinctly large vesicles. This texture is likely due to the heterogeneous bubble nucleation at the surface of the lithic fragment (e.g. Gardner and Denis, 2004). (c) BSE image of a quartz crystal in trachyte pumice. The dissolution rim of the quartz likely formed as a result of heating. (d) BSE image of a quartz xenocryst with a reaction rim composed mostly of clinopyroxene, hosted in basalt. **(e)** BSE image of amphibole pseudomorph in trachyte pumice sample 18CW100–28. The heating of the trachyte reservoir caused by rejuvenation of mafic magma may have triggered trachyte-hosted amphiboles to dissolve into the observed pseudomorphs.

while affixed to the calcic core of a plagioclase phenocryst was made by Izbekov et al. (2004) at Karymsky volcano. The strong evidence supporting contemporaneous rim formation in crystal clots justifies our use of diffusion timescales from clinopyroxene to calculate growth rates for plagioclase phenocrysts and amphibole reaction rims.

Minerals within multi-phase crystal clots share similar chemical changes between core and rim compositional zones. This may suggest that the cores originally were part of the same magma storage system, then experienced a change in the conditions of the magmatic system simultaneously. One crystal clot from a basaltic scoria sample (Fig. 10a) depicts a shared boundary between clinopyroxene, plagioclase, and amphibole. In this clot, the outermost rims of clinopyroxene and plagioclase seemingly correspond with the amphibole reaction rim, and, relative to their cores, have lower Mg# and anorthite content, respectively. Another crystal clot (Fig. 10b) exhibits plagioclase and clinopyroxene phenocrysts with a shared core-rim boundary. Fig. 10c shows a crystal clot where the distinct boundary in a normally zoned clinopyroxene may be traced across to the demarcation separating the amphibole phenocryst core from its reaction rim.

The presence of the shared boundary traceable across attached phenocrysts provides a unique opportunity to determine rates of plagioclase growth and amphibole reaction rim formation. Our diffusion model for the boundaries in clinopyroxene provides a timescale estimate for shared rims in the attached plagioclase and/or amphibole from

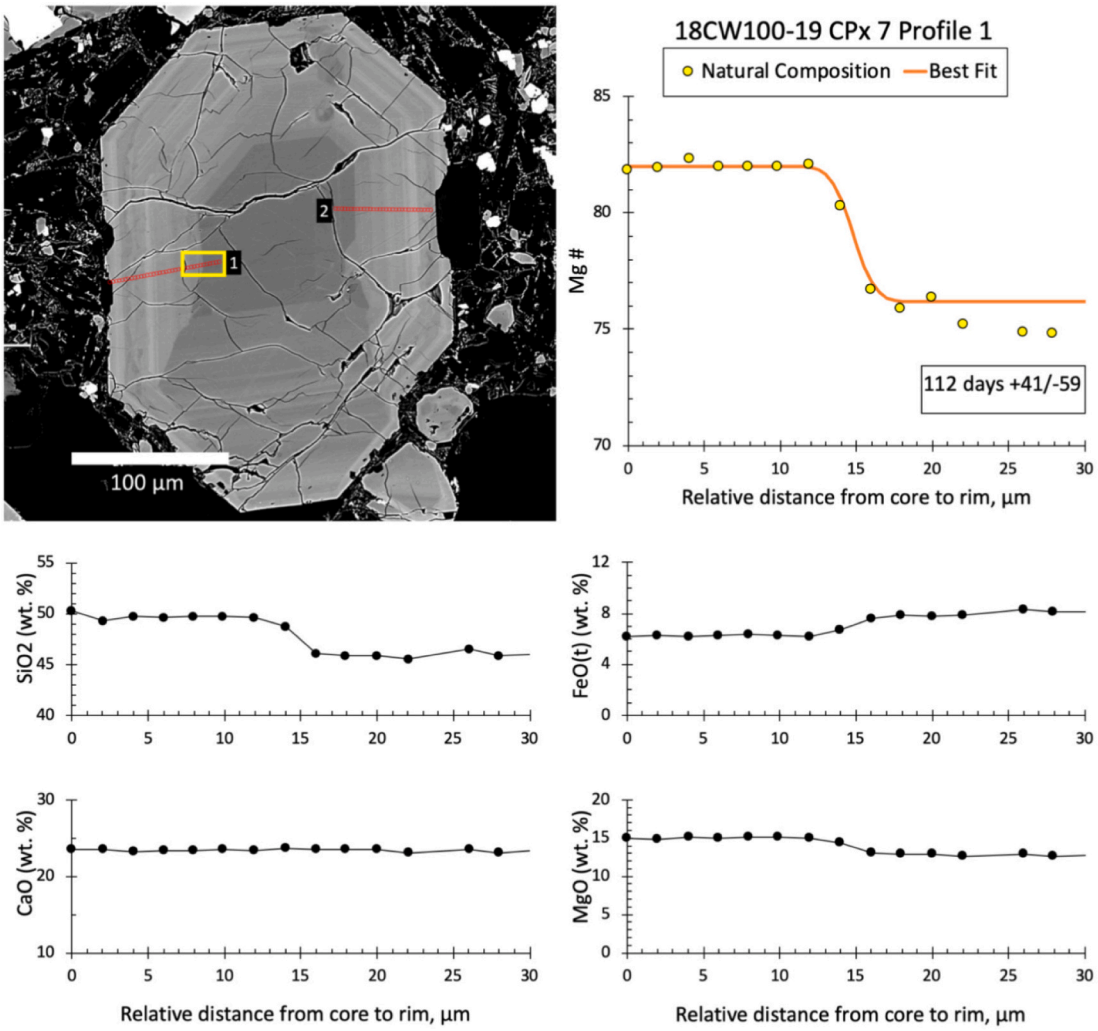

Fig. 7. (Top left) back-scattered electron image of a clinopyroxene phenocryst showing the locations of electron microprobe transects by red lines. The location of the corresponding transects from EPMA analyses and results of diffusion modeling with the calculated age of the chemical boundary is indicated by the yellow box.

which we can calculate natural apparent growth rates.

With the textural and chemical evidence shown by the zoned crystal clots supporting our hypothesis of contemporaneous rim formation, we utilized diffusional timescales in clinopyroxene to calculate applicable growth rates for the outermost rims of plagioclase ($1.7 \pm 0.99 \times 10^{-6}$ um/s). We utilize the shortest rim width of plagioclase phenocrysts, assuming that wider sections are products of either faster growth rates due to crystallographic preference or of the crystal having been cut obliquely. Our calculated plagioclase growth rate is comparable to published growth rates of 3.5×10^{-6}–6.06×10^{-5} um/s (Larsen, 2005). Additionally, the work of Kirkpatrick (1977), which studies the processes of basaltic crystallization at Hawaiian lava lakes, describes plagioclase growth rates perpendicular to (010) to range from 1.7×10^{-6} to 1.1. X 10^{-5} um/s. It is assumed that crystal growth occurs more rapidly than the internal Fe—Mg interdiffusion, thus, our plagioclase growth rate calculated from clinopyroxene diffusion timescales may be an underestimate of the true rate.

We additionally used crystal clots to calculate the rate of reaction rim formation in amphiboles to be $2.8 \pm 0.47 \times 10^{-6}$ um/s. We use a calculated mean width for amphibole reaction rims, after the rim-width-measuring methodology of De Angelis et al. (2013). The implication of amphibole reaction rims is that an original crystalline rim must form before subsequently breaking down into a reaction rim. Our rim formation rate in natural amphiboles thus serves as a maximum, in that the reaction rims may have formed significantly more rapidly during magma ascent or shallow storage, when magmas exited the range of amphibole stability. It is due to these uncertainties that we do not utilize our amphibole reaction rim growth rate to independently determine magmatic timescales using growth rate chronometry.

3.6. Growth rate chronometry

Using the timescales of clinopyroxene diffusion, and relating these to the growth rate of shared rims in crystal clots, we infer additional timescales from rim width of plagioclase crystals. Eighteen plagioclase rims were measured and had widths ranging from 7.8 to 36.0 um, corresponding to growth ranging from 43 to 200 days. Overall, both clinopyroxene diffusion and plagioclase growth rate chronometry result in similarly short timescales ranging weeks to months before the cessation of the eruption (Fig. 8; Fig. 9d).

Growth rate chronometry may be a particularly useful tool to constrain timescales of magma processes. Computing magmatic timescales from growth rate chronometry is significantly faster than performing diffusion studies, due to the fact that growth rate chronometry requires only phenocryst imaging, while diffusion studies require detailed quantitative core-rim transects. The analytical time and cost required for growth rate chronometry is nearly negligible, thereby allowing us to rapidly analyze many crystals and constrain the

Table 1
Results from diffusion modeling in clinopyroxene.

Sample ID	Clino- pyroxene	Profile #	Zonation type	Timescale	(+) Uncertainty	(−) Uncertainty
	Crystal ID			Days	Days	Days
Basaltic Scoria						
18CW100-10A	1	1	Normal	46	16	−25
18CW100-10A	2	1	Normal	77	27	−42
18CW100-10A	3	3	Normal	36	12	−21
18CW100-10A	4	2	Normal	8	3	−4
18CW100-13B	1	5	Reversed	11	6	−2
18CW100-13B	5	1	Reversed	180	64	−98
18CW100–19	6	1	Normal	96	34	−53
18CW100–19	7	1	Normal	112	41	−59
18CW100–19	8	1	Reversed	96	34	−53
18CW100–19	9	1	Normal	55	19	−30
18CW100–19	10	2	Normal	145	51	−80
18CW100–19	11	3	Reversed	10	3	−7
18CW100–19	12	3	Normal	23	8	−13
18CW100–24	1	2	Reversed	11	4	−6
18CW100–24	2	1	Reversed	174	61	−96
18CW105–3	1a	1	Normal	8	3	−4
18CW105–3	2	3	Reversed	44	16	−24
18CW105–3	3	1	Normal	1	0	−2
18CW105–3	4	2	Reversed	19	6	−11
18CW105–3	5	2	Reversed	84	30	−46
18CW105–3	6	2	Reversed	6	2	−4
18CW105–3	7	5	Normal	96	34	−53
18CW105–3	CC1	3	Normal	43	15	−24
18CW105–3	CC2	3	Normal	59	21	−33
18CW105–3	CC3	2	Normal	117	41	−64
Mafic Enclave						
18CW105-1B	2	2	Normal	59	21	−32
Trachyandesite						
18CW100–6	(CC) 1	4	Reversed	90	32	−49
18CW100–6	3	4	Normal	178	79	−58
18CW105-1A	3	2	Normal	103	36	−58

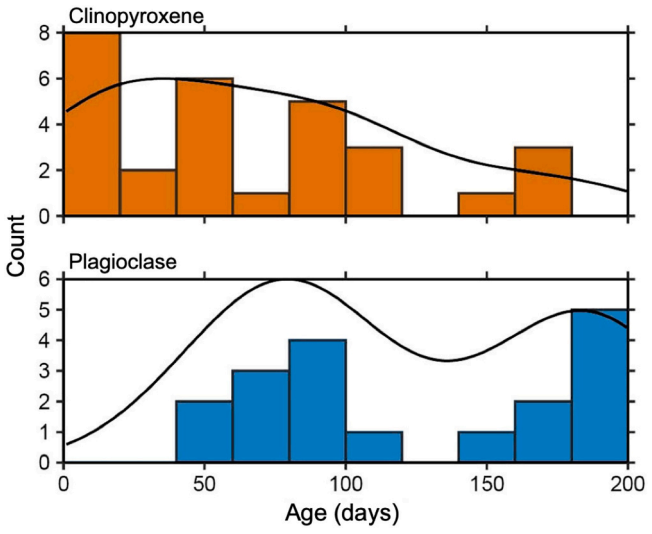

Fig. 8. Histograms of resulting timescales from clinopyroxene diffusion chronometry and plagioclase growth rate chronometry. Curves above the histograms are kernel density estimates utilizing 30-day bin widths to accommodate for average uncertainties in the timescale results.

timescales of magmatic processes more efficiently than with diffusion chronometry. Our plagioclase timescales largely mirror our clinopyroxene diffusion timescales: lacking any distinctive long or short timescale populations (Fig. 8). This provides us with additional confidence that we do not miss a population in the limited number of analyzed clinopyroxene crystals. In the future, growth rate chronometry may aid in analyses of the timescales of magmatic processes in addition to the well-established diffusion chronometry.

4. Discussion

4.1. Sharp chemical boundaries

The volcanic products of 2016–2017 eruption of Bogoslof include phenocrysts of clinopyroxene, plagioclase, and amphibole, all of which exhibit compositional and/or textural zoning which separates their cores from the distinct rims. The growth and stability of minerals are controlled by multiple factors, including but not limited to changes in temperature, pressure, magma composition, volatile content, and oxidation state. Evidence from multi-phase crystal clots indicates that the distinct boundaries in all three mineral phases formed contemporaneously (Fig. 10). By synthesizing the wealth of knowledge from petrological experiments, we may determine one single process which caused all three mineral phases to react and form new rims. Below, we list a variety of theoretical magmatic processes which may be responsible for observed sudden changes in the mineral phases. One by one, we will rule out the magmatic processes until we are left with one simple explanation: the sharp compositional gradients found between crystal cores and outer rims in clinopyroxene and plagioclase, along with the contemporaneous breakdown of amphibole, are best explained by the rapid ascent-driven decompression of hot basaltic magma.

Heating caused by magma recharge is not consistent with the continuous growth of sodic plagioclase and Fe-rich clinopyroxene rims and apparent absence of dissolution boundaries (Waters et al., 2015). We also rule out the possibility of rapid cooling, as this would not lead to

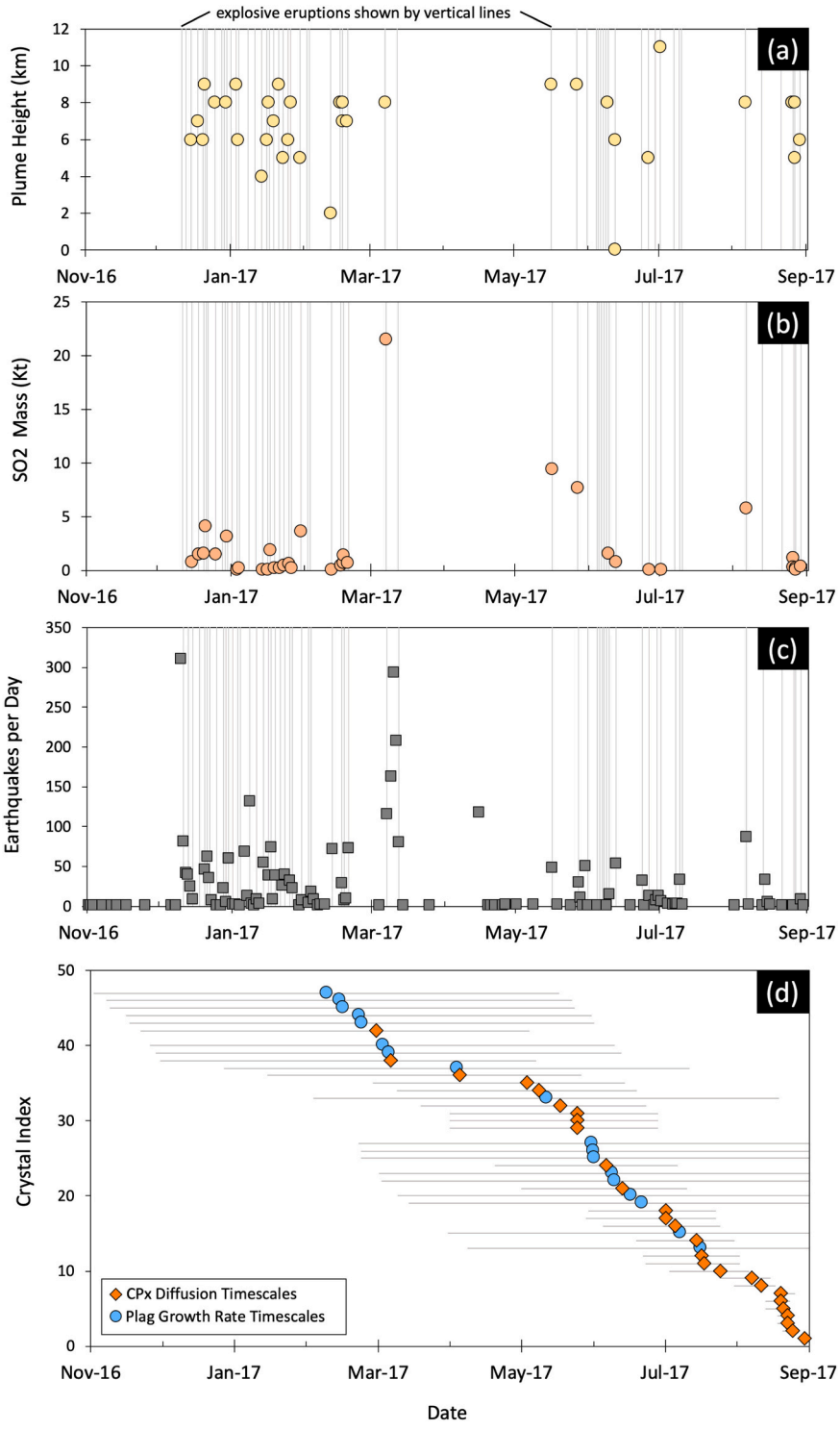

Fig. 9. Compiled interdisciplinary time series results and observations over the course of the 2016–2017 Bogoslof eruption. (a) Shows recorded plume heights (Schneider et al., 2020), (b) depicts measured SO_2 mass flux (Lopez et al., 2020), and (c) shows the number of earthquakes per day (Wech et al., 2018). (d) Shows the results of this study, including timescales from clinopyroxene diffusion and plagioclase growth rate chronometry. Resulting timescales were subtracted from the date the samples erupted in order to correlate diffusion timescales with interdisciplinary monitoring data. Error bars for clinopyroxene diffusion ages are based on uncertainty in modeling temperature. Error bars for plagioclase growth rate timescales are calculated based on uncertainty in measured rim widths.

amphibole decomposition. Similarly, a rapid transfer of crystal cargo from a high-temperature domain to a low-temperature environment with evolved melt composition would not affect the stability of amphibole. Although change of melt composition due to the assimilation of trachyte cannot be excluded, and therefore it could have potentially affected compositions of clinopyroxenes and plagioclases, this would not affect the stability of amphiboles (King et al., 2018). While gradual change of melt composition due to cooling and protracted crystallization could theoretically explain a difference between core and rim compositions, it is not consistent with the observed sharp compositional boundaries, as extended crystallization would likely produce non-stepwise compositional gradients.

With evidence suggesting that the amphibole reaction rims may have formed contemporaneously with the outer rims of clinopyroxene and plagioclase, an explanation for the source of the abrupt change may be recorded in the composition and textures of amphibole breakdown rims. The amphibole reaction rims possess a microlite mineral assemblage of plagioclase, clinopyroxene, orthopyroxene, and Fe—Ti oxides. The experimental results of De Angelis et al. (2013) and Browne and Gardner (2006) attribute the crystallization of clinopyroxene in reaction rims to

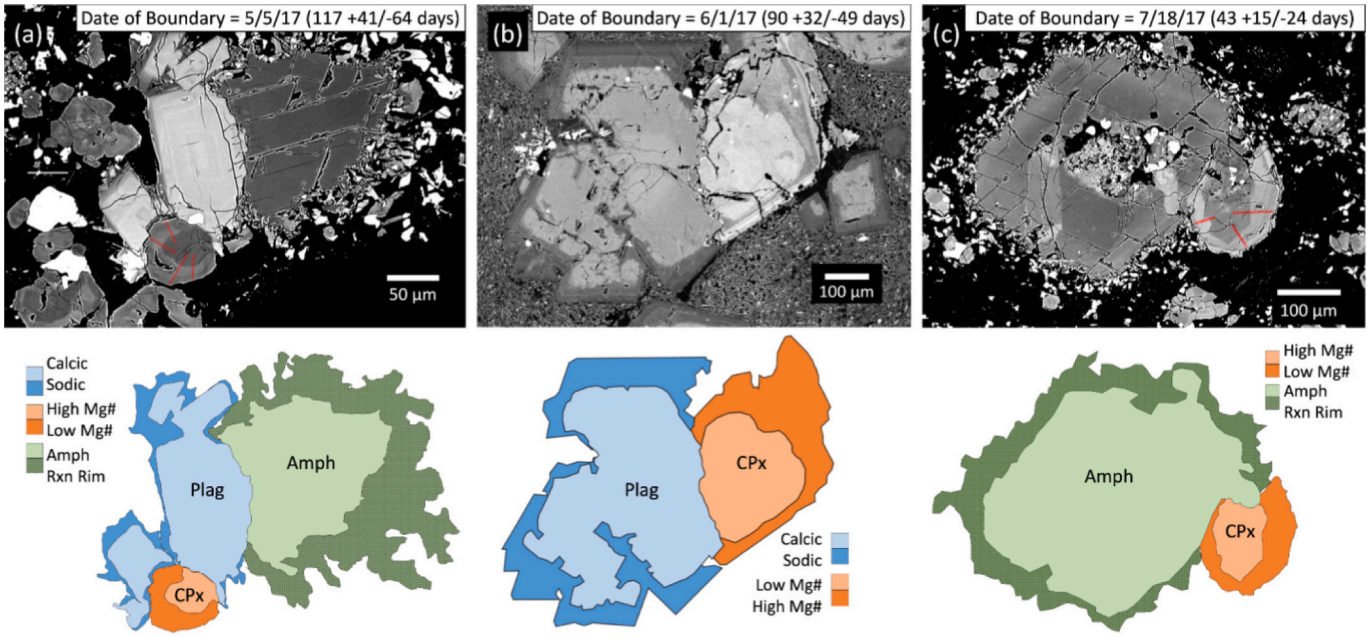

Fig. 10. BSE images of crystal clots with compositional / textural boundaries, which can be traced across clinopyroxene (CPx), plagioclase (Plag), and amphibole (Amph). The outer rims of clinopyroxene and plagioclase correlate with amphibole reaction rims (Rxn Rim). Both (a) and (c) are found in basalt, while (b) is found in trachyandesite. Red lines on BSE images represent measured EPMA core-rim transects taken across distinct zonal boundaries in clinopyroxene. BSE images in (a) and (b) are stitched together from two separate BSE images in order to visualize detailed zoning in all mineral phases, which is why plagioclase appears brighter than the other phases in (a). (For interpretation of the references to colour in this figure legend, the reader is referred to the web version of this article.)

heating events, and orthopyroxene to decompression. While the complexity of natural amphiboles often exceeds those of experimental studies, we suggest that the presence of both clinopyroxene and orthopyroxene in observed reaction rims may indicate that Bogoslof amphiboles in basalts experienced a combination of ascent-driven decompression and slight change in melt composition prior to eruption, which may be attributed to the rejuvenation and minor incorporation of older trachytic magma (Fig. 6; Fig. 11). Notably, amphibole reaction rims display a variety of textures: Some display small-structured microlites near the edge of the amphibole, with larger-structured microlites farther away, and some display the exact opposite, with larger structure near the amphibole and a sharp change to smaller

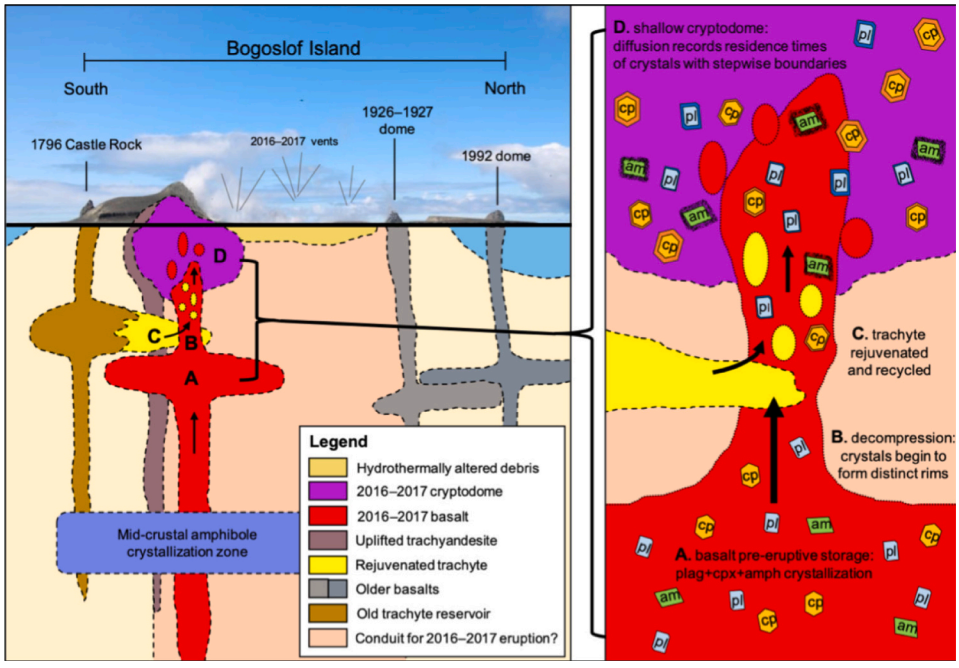

Fig. 11. Conceptual cross-section cartoon of Bogoslof, after Loewen et al. (2019). Details regarding locations A-D are shown to the right. A) Is the shallow basalt pre-eruptive storage area, where plagioclase (pl), clinopyroxene (cp) and amphibole (am) begin/continue to crystallize. This is likely where the relatively low Al_2O_3 zones grew in amphibole. B) Depicts ascent-driven decompression of the magma, triggering abrupt compositional changes in clinopyroxene and plagioclase, and bringing amphibole out of its range of stability, thereby forming breakdown rims. C) Shows where the old trachyte reservoir is partially reheated and recycled. This is where Fe—Ti oxides re-equilibrate to the high basalt temperatures, and magmas mingled to create the observed hand samples, xenocrysts, and crystal textures (Fig. 6). This could also be where amphiboles hosted in the trachyte are turned into pseudomorphs. D) Is the shallow cryptodome where diffusion across newly formed stepwise boundaries records the residence times of the crystals. The range in diffusion ages indicate that magma continually rejuvenated the cryptodome storage area over the weeks to months before the cessation of the eruption, meaning that the products of each eruptive episode possess crystal cargo which exhibit a spectrum of ages across their chemical zones, depending on how long they spent in area D before erupting to the surface. Figure is schematic and is not drawn to scale.

structure farther away (Fig. 4).

While most of the outer rims of amphiboles have broken down, some amphiboles retain an area of lower Al_2O_3 rims. Transects across the compositional boundaries in such amphiboles reveal that cores are high Al_2O_3 relative to the rims. The cores and rims additionally exhibit inverted relationships between MgO and FeO (Loewen et al., 2019). The boundary separating high Al_2O_3 cores from low Al_2O_3 rims indicate that amphibole phenocrysts with this distinct compositional zoning initially crystallized in a high pressure reservoir and were later brought to a second reservoir of lower pressure where the low Al_2O_3 rims formed, similar to the observed compositional variations at Bezymianny Volcano, Kamchatka (Turner et al., 2013). The shared boundaries between the distinct rims of clinopyroxene and plagioclase with amphibole reaction rims indicate that the Al_2O_3 zonation in amphibole phenocrysts records events before the formation of stepwise boundaries in other mineral phases. We suggest that the high Al_2O_3 cores of amphiboles formed in a mid crustal storage area, and that the presence of lower Al_2O_3 zones record evidence for the path of magma ascent into a second storage area of slightly lower pressure than that of the mid-crustal reservoir (Fig. 11). These amphiboles crystallized low Al_2O_3 zones while clinopyroxene and plagioclase crystallized in the second storage area, and all phases then formed their outermost rims (including amphibole reaction rims) during final ascent-driven decompression (McCanta et al., 2006). Ultimately, this ascent of magma led to either immediate eruption or temporary stalling in shallow cryptodomes for weeks–months. The presence of amphiboles with low Al_2O_3 rims which lack the outermost breakdown rim can be explained by rapid ascent and eruption, suggesting that these amphiboles did not reside at a shallow depth long enough to begin the breakdown process.

An abrupt decrease in pressure triggered by magma ascent followed by a residence at a shallow depth remains the only possible explanation for the contemporaneous formation of sodic plagioclase, Fe-rich clinopyroxene, and amphibole reaction rims. Rapid decompression drives water out of the melt, triggering simultaneous crystallization of stable mineral phases and decomposition of amphiboles. Decompression of this nature is most commonly caused by the vertical ascent of magma through the crust. Temperature of the magma remains relatively constant, causing the system to leave the field of amphibole stability as pressure decreases. Meanwhile, stable phases continue to crystallize in a chemically distinct composition. Diffusion across compositionally contrasting zones of stable phases may be used to estimate residence times of crystals in the shallow pre-eruptive cryptodome.

As conceptualized in Fig. 11, the basalt continually replenished a shallow storage chamber, forming cryptodomes before subsequently erupting to the surface. The continuous injection of basalt into the shallow cryptodome storage area, coupled with the rejuvenation and subsequent mingling of trachytic magma, is likely responsible for the presence of both normally and reversely zoned clinopyroxene crystals. The deeper clinopyroxene crystals hosted in the fresh basalt experienced rapid decompression, triggering the formation of distinctly lower Mg# rims (normal zoning), while shallow clinopyroxene cores hosted in the shallow cryptodome area experienced heating from the fresh basalt and formed higher Mg# rims (reverse zoning). These processes occurred nearly simultaneously, and thus our diffusion models result in similar timescales, regardless of chemical zonation (Table 1).

4.2. Implications of diffusion chronometry results

Accounting for the range of temperatures associated with the uncertainty of Fe—Ti thermometry, the lowest temperature suggests that the oldest diffusion ages may even correspond to late November/early December 2016 (Fig. 9). Knowing the timing of eruption for samples allows us to date the individual zones in magmatic phenocrysts, as pre-eruptive magmatic processes trigger the formation of new, chemically distinct rims, and diffusion between the core and subsequent rims begins immediately.

Our diffusion results suggest that the zonal boundaries within the phenocrysts of the 2016–2017 eruption of Bogoslof formed in the weeks to months prior to the cessation of the eruption. Similarly short timescales have been observed in both clinopyroxene and orthopyroxene diffusion studies. For example, Kilgour et al. (2014) present diffusion timescale results from both clinopyroxene and orthopyroxene erupted at Ruapehu volcano, timescales of which also range weeks to months prior to eruption. Saunders et al. (2012b) use diffusion in orthopyroxene to study magmatic timescales leading up to the 1980–1986 series of eruptions at Mount St. Helens, again establishing that the time elapsed between final rim formation and eruption ranges from days to months. It is notable that the eruptions of Ruapehu and Mount Saint Helens behaved similarly to the most recent eruption of Bogoslof, in that all three eruptions formed domes/cryptodomes, and additionally all display short diffusion timescales recorded in their erupted products. We interpret these short timescales at Bogoslof as evidence that the distinct boundaries within the main mineral phases were not inherited from prior eruptions, but rather record changes that occurred during the 2016–2017 period of activity.

Samples used in this study were collected from the surface <1 year after the end of the eruption, thus, we assume that all basalt and trachyte samples used in this study are the products of the final explosive event on August 30, 2017. Our diffusion models in clinopyroxene result in a value of days since the chemical core-rim boundary was formed. By subtracting these values from the day the samples were erupted, we may approximate the dates when the magmatic processes that created the distinct boundaries occurred. Our clinopyroxene diffusion modeling ages indicate that changes in the magmatic system may have begun around March 2017, seemingly overlapping with increases in both SO_2 mass flux (Lopez et al., 2020) and seismicity (Wech et al., 2018) that occurred during a pause in eruptive events around March (Fig. 9a and b). The correlation between gas monitoring data and our diffusion timescales indicates that degassing of magma during ascent and shallow emplacement is responsible for the observed increase in SO_2 and the formation of new distinct crystal rims. It is reasonable to infer that the increased seismic activity, which overlaps with other monitoring data and our results, was also triggered by the movement of magma through the crust and into the shallow cryptodome.

4.3. Trachyte rejuvenation and shallow magma emplacement

Volcanic eruptions are frequently triggered by the injection of mafic magma into an upper crustal magma storage area (Murphy et al., 1998; Eichelberger et al., 2000; Eichelberger and Izbekov, 2000; Leonard et al., 2002; Edmonds et al., 2010). We suggest that for the most recent eruption of Bogoslof, the repetitive decompression and subsequent emplacement of fresh mafic magma into a shallow magma reservoir can explain our observations. The magma experienced ascent-driven decompression which created distinct rims in mineral phases. Distinct chemical zoning ubiquitous in samples reflects magma stalling in this region, and timescales estimated from diffusion and crystal growth rate chronometry show that this occurred throughout the course of the 2016–2017 eruption (Fig. 9). During the eruption, basalt rejuvenated and recycled old trachytic material. In addition to macroscopic hand samples, further evidence to support the mingling of basalt and trachyte are trace quartz xenocrysts with reaction rims found in basalt (Fig. 6d). The mingling of magmas additionally created a bimodal population of normally and reversely zoned crystals.

The second line of evidence supporting the rejuvenation of trachyte by mafic magma is the composition of the trachyte pumice. The oldest recorded eruption at Bogoslof of Castle Rock in 1796–1804 was of a nearly identical composition to the 2016–2017 trachyte (Loewen et al., 2019). The high crystallinity of the recently erupted trachyte further suggests that the basalt which dominated the 2016–2017 and other historical eruptions at Bogoslof reheated and rejuvenated unerupted Castle Rock magma (Fig. 6; Fig. 11).

The presence of amphibole pseudomorphs in trachyte pumice may also support the heating of the trachyte by the intrusion of fresh magma, as experimental results show that heating of amphiboles favors the rapid formation of pseudomorphs (De Angelis et al., 2013).

Additionally, temperature calculations on Fe—Ti oxide pairs in the trachyte from Loewen et al. (2019) indicate a high temperature expected of amphibole bearing basalts (980–1056 °C), while our two-feldspar thermometer calculations result in temperatures approximately 100–200 °C cooler. This can be explained by comparing the rates of re-equilibration of Fe—Ti oxides and feldspars.

Volcanic products of trachytic composition were not observed in January, March, or May distal ashfall samples. This suggests that the trachyte only erupted toward the end of the 2016–2017 eruption. Loewen et al. (2019) use this as evidence for magma rejuvenation, where the highly crystalline subsolidus trachyte, possibly residual from the 1796 eruption, was reheated in the first weeks–months of the eruption and began mingling and erupting with juvenile basalt in the final months of the eruption. The first weeks–months of the eruption serve as a sufficient window of time for the Fe—Ti oxides in the trachyte to thermally re-equilibrate to basaltic temperatures (Venezky and Rutherford, 1999).

Given that feldspars do not thermally re-equilibrate as rapidly as Fe—Ti oxides, we interpret the difference in resulting temperatures between the two as further evidence to support heating of the trachyte. The Fe—Ti oxides re-equilibrated to the temperature of the intruding mafic magma, while the feldspars record an intermediate temperature between that of the hot juvenile basalt and that of the trachyte reservoir before experiencing any heating.

5. Conclusions

The 2016–2017 eruption of Bogoslof produced basalts, which have a mineral assemblage including plagioclase, clinopyroxene, and amphibole. All three of the dominant mineral phases exhibit sharp chemical boundaries, which can be cross-correlated in plagioclase-clinopyroxene-amphibole crystal clots, thereby suggesting that the distinct zones in the three phases formed simultaneously. At these shared boundaries, clinopyroxene continued growing, but suddenly changed composition from Mg# 81.7 ± 5.8 to 72.9 ± 3.0. Plagioclase continued growing, but abruptly changed composition from $An_{82.5\pm1.4}$ to $An_{61.3\pm5.7}$. At approximately the same time, amphiboles became unstable and formed reaction rims. The continued growth of clinopyroxene and plagioclase, their compositional changes, as well as instability of amphibole allowed us to narrow down the possible origin of the shared boundaries and propose that they were formed as a result of rapid, ascent-driven decompression, followed by crystallization at a shallow cryptodome depth, where magma accumulated prior to explosions and chemical diffusion recorded residence times of crystals.

The presence of ilmenite-magnetite pairs in the associated trachyte, which was fused and thermally re-equilibrated with the host basalt, allowed us to put constraints on the temperature of the basaltic magma. We were able to model Mg—Fe interdiffusion across the distinct zones in clinopyroxenes and to determine their ages, which ranged from weeks to months. Samples analyzed in this study were erupted during the final explosive episode on August 30, 2017, when the diffusion in resident crystals stopped. Using our timescales from clinopyroxene diffusion chronometry, we were able to date the shared boundaries in multi-phase crystal clots, which, coupled with rim width measurements, allowed us to calculate a plagioclase rim growth rate of $1.7 \pm 0.99 \times 10^{-6}$ um/s, which is comparable to prior estimates for Karymsky magma system (Izbekov et al., 2004) and experimental results (Larsen, 2005). In addition, we estimated the rate of amphibole reaction rim formation to be $2.8 \pm 0.47 \times 10^{-6}$ um/s. Importantly, in the case of the 2016–2017 Bogoslof eruption, the amphibole reaction rims formed in response to decompression, not temperature increase, which is suggested by the simultaneous and continuous growth of plagioclase and clinopyroxene.

In summary, a rich mineralogy, the known age of eruptive products, and independent constraints for the temperature of the 2016–2017 Bogoslof magma provided us with a unique opportunity to identify the processes responsible for the formation of chemical boundaries and to determine their timing. Both diffusion chronometry and growth rate chronometry serve as powerful tools to analyze individual zones in phenocrysts by constraining the timescales of the magmatic processes which formed them. By combining our compositional and temporal petrologic information with the data of other disciplines, we may perform petrologic monitoring in order to aid in the interpretation of interdisciplinary monitoring signals. Our results indicate that changes in traditional monitoring data, such as seismicity and volcanic degassing, directly relate to perturbations in the conditions of the magmatic system (Kahl et al., 2013).

CRediT authorship contribution statement

Jamshid Moshrefzadeh: Conceptualization, Methodology, Formal analysis, Investigation, Writing – original draft, Writing – review & editing, Visualization. **Pavel Izbekov:** Conceptualization, Methodology, Formal analysis, Resources, Writing – review & editing, Supervision, Funding acquisition. **Matthew Loewen:** Investigation, Resources, Writing – review & editing, Supervision. **Jessica Larsen:** Resources, Writing – review & editing, Supervision, Funding acquisition. **Sean Regan:** Methodology, Supervision.

Declaration of Competing Interest

The authors declare that they have no known competing financial interests or personal relationships that could have appeared to influence the work reported in this paper.

Data availability

Data analyzed in this article are provided in the supplementary material.

Acknowledgements

We would like to thank Christopher Waythomas and Kristi Wallace for collecting 2016–2017 Bogoslof samples and documenting the deposits. We also thank Nathan Graham for assistance with microprobe work at the UAF AIL. The 2018 and 2019 field campaigns were successful due to the professional assistance from the captain and crew of R/V Tiglax of the U.S. Fish & Wildlife Service. We greatly appreciate the feedback and guidance from Allison Gale and Fidel Costa. This manuscript benefited immensely from constructive discussions and comments by James Gardner, Dawn Ruth, Michelle Coombs, and anonymous reviewers.

This project was supported by the Volcano Hazards Program of The U.S. Geological Survey through the Alaska Volcano Observatory, NSF ICER 1855126, and by Teaching Assistantship through the Department of Geosciences at UAF. Any opinions, findings, and conclusions or recommendations expressed in this material are those of the author(s) and do not necessarily reflect the views of the National Science Foundation. This journal article has been peer reviewed and approved for publication consistent with USGS Fundamental Science Practices. With Bureau approval, The U.S.Geological Survey fully stands behind the opinions, conclusions, and interpretations in this paper. Any use of trade, firm, or product names is for descriptive purposes only and does not imply endorsement by the U.S. Government.

Appendix A. Supplementary data

Supplementary data to this article can be found online at https://doi.org/10.1016/j.jvolgeores.2022.107741.

References

Abramoff, M.D., 2007. ImageJ as an image processing tool and library. Microsc. Microanal. 13 https://doi.org/10.1017/s1431927607079652.

Allan, A.S.R., Morgan, D.J., Wilson, C.J.N., Millet, M.-A., 2013. From mush to eruption in centuries: assembly of the super-sized Oruanui magma body. Contrib. Mineral. Petrol. 166, 143–164. https://doi.org/10.1007/s00410-013-0869-2.

Bacon, C., Hirschmann, M., 1988. Mg/Mn partitioning as a test for equilibrium between coexisting Fe-Ti oxides. Am. Mineral. 73, 57–61.

Browne, B., Gardner, J., 2006. The influence of magma ascent path on the texture, mineralogy, and formation of Hornblende Reaction Rims. Earth Planet. Sci. Lett. 246, 161–176. https://doi.org/10.1016/j.epsl.2006.05.006.

Chakraborty, S., 2008. Diffusion in solid silicates: A tool to track timescales of processes comes of age. Annu. Rev. Earth Planet. Sci. 36, 153–190. https://doi.org/10.1146/annurev.earth.36.031207.124125.

Charlier, B., Morgan, D., Wilson, C., Wooden, J., Allan, A., Baker, J., 2012. Lithium concentration gradients in feldspar and quartz record the final minutes of magma ascent in an explosive supereruption. Earth Planet. Sci. Lett. 319-320, 218–227. https://doi.org/10.1016/j.epsl.2011.12.016.

Coombs, M.L., Wech, A.G., Haney, M.M., Lyons, J.J., Schneider, D.J., Schwaiger, H.F., Wallace, K.L., Fee, D., Freymueller, J.T., Schaefer, J.R., Tepp, G., 2018. Short-term forecasting and detection of explosions during the 2016–2017 eruption of Bogoslof Volcano, Alaska: Frontiers. Earth Sci. 6 https://doi.org/10.3389/feart.2018.00122.

Coombs, M., Wallace, K., Cameron, C., Lyons, J., Wech, A., Angeli, K., Cervelli, P., 2019. Overview, chronology, and impacts of the 2016–2017 eruption of Bogoslof Volcano, Alaska. Bull. Volcanol. 81 https://doi.org/10.1007/s00445-019-1322-9.

Costa, F., Dungan, M., 2005. Short time scales of magmatic assimilation from diffusion modeling of multiple elements in Olivine. Geology 33, 837. https://doi.org/10.1130/g21675.1.

Costa, F., Dohmen, R., Chakraborty, S., 2008. Time Scales of Magmatic Processes from Modeling the Zoning Patterns of Crystals. Rev. Mineral. Geochem. 69, 545–594. https://doi.org/10.2138/rmg.2008.69.14.

Costa, F., Shea, T., Ubide, T., 2020. Diffusion Chronometry and the timescales of Magmatic Processes. Nat. Rev. Earth Environ. 1, 201–214. https://doi.org/10.1038/s43017-020-0038-x.

De Angelis, S.H., Larsen, J., Coombs, M., 2013. Pre-eruptive magmatic conditions at Augustine Volcano, Alaska, 2006: Evidence from amphibole geochemistry and textures. J. Petrol. 54, 1939–1961. https://doi.org/10.1093/petrology/egt037.

Demets, C., Gordon, R.G., Argus, D.F., Stein, S., 1994. Effect of recent revisions to the geomagnetic reversal time scale on estimates of current plate motions. Geophys. Res. Lett. 21, 2191–2194. https://doi.org/10.1029/94gl02118.

Dimanov, A., Wiedenbeck, M., 2006. (Fe,Mn)-Mg interdiffusion in natural diopside: Effect of PO2. Eur. J. Mineral. 18, 705–718. https://doi.org/10.1127/0935-1221/2006/0018-0705.

Dohmen, R., Chakraborty, S., Becker, H.-W., 2002. Si and O diffusion in olivine and implications for characterizing plastic flow in the mantle. Geophys. Res. Lett. 29 https://doi.org/10.1029/2002gl015480.

Dohmen, R., Faak, K., Blundy, J.D., 2017. Chronometry and Speedometry of Magmatic Processes using Chemical Diffusion in Olivine. Plagioclase Pyroxenes Rev. Mineral. Geochem. 83, 535–575. https://doi.org/10.2138/rmg.2017.83.16.

Donovan, J.J., Lowers, H.A., Rusk, B.G., 2011. Improved electron probe microanalysis of trace elements in quartz. Am. Mineral. 96, 274–282. https://doi.org/10.2138/am.2011.3631.

Drouin, D., Couture, A.R., Joly, D., Tastet, X., Aimez, V., Gauvin, R., 2007. CASINO V2.42—A Fast and Easy-to-use Modeling Tool for Scanning Electron Microscopy and Microanalysis Users. Scanning 29, 92–101. https://doi.org/10.1002/sca.20000.

Druitt, T.H., Costa, F., Deloule, E., Dungan, M., Scaillet, B., 2012. Decadal to monthly timescales of magma transfer and reservoir growth at a caldera volcano. Nature 482, 77–80. https://doi.org/10.1038/nature10706.

Edmonds, M., Aiuppa, A., Humphreys, M., Moretti, R., Giudice, G., Martin, R.S., Herd, R. A., Christopher, T., 2010. Excess volatiles supplied by mingling of mafic magma at an andesite arc volcano: Geochemistry. Geophys. Geosyst. 11 https://doi.org/10.1029/2009gc002781.

Eichelberger, J.C., Izbekov, P.E., 2000. Eruption of andesite triggered by Dyke Injection: Contrasting cases at Karymsky Volcano, Kamchatka and Mt Katmai, Alaska: Philosophical Transactions of the Royal Society of London. A: Math. Phys. Eng. Sci. 358, 1465–1485. https://doi.org/10.1098/rsta.2000.0599.

Eichelberger, J.C., Chertkoff, D.G., Dreher, S.T., Nye, C.J., 2000. Magmas in collision: Rethinking chemical zonation in Silicic magmas. Geology 28, 603. https://doi.org/10.1130/0091-7613(2000)28<603:micrcz>2.0.co;2.

Fee, D., Lyons, J., Haney, M., Wech, A., Waythomas, C., Diefenbach, A.K., Lopez, T., Eaton, A.V., Schneider, D., 2019. Seismo-acoustic evidence for vent drying during shallow submarine eruptions at Bogoslof Volcano, Alaska. Bull. Volcanol. 82 https://doi.org/10.1007/s00445-019-1326-5.

Fournelle, J.H., Marsh, B.D., Myers, J.D., 1994. Age, character, and significance of Aleutian Arc Volcanism. Geol. Alaska 723–757. https://doi.org/10.1130/dnag-gna-g1.723.

Gansecki, C., Lee, R.L., Shea, T., Lundblad, S.P., Hon, K., Parcheta, C., 2019. The tangled tale of Kīlauea's 2018 eruption as told by geochemical monitoring. Science 366. https://doi.org/10.1126/science.aaz0147.

Gardner, J.E., Denis, M.-H., 2004. Heterogeneous bubble nucleation on Fe-Ti oxide crystals in high-silica rhyolitic melts. Geochim. Cosmochim. Acta 68, 3587–3597. https://doi.org/10.1016/j.gca.2004.02.021.

Gerlach, D.C., Grove, T.L., 1982. Petrology of Medicine Lake Highland volcanics: Characterization of endmembers of magma mixing. Contrib. Mineral. Petrol. 80, 147–159. https://doi.org/10.1007/bf00374892.

Ghiorso, M.S., Evans, B.W., 2008. Thermodynamics of Rhombohedral Oxide Solid Solutions and a Revision of the FE-TI Two-Oxide Geothermometer and Oxygen-Barometer. Am. J. Sci. 308, 957–1039. https://doi.org/10.2475/09.2008.01.

Gualda, G.A., Pamukcu, A.S., Ghiorso, M.S., Anderson, A.T., Sutton, S.R., Rivers, M.L., 2012. Timescales of quartz crystallization and the longevity of the Bishop Giant Magma Body. PLoS One 7. https://doi.org/10.1371/journal.pone.0037492.

Hollister, L., Hargraves, R., 1970. Compositional sector-zoning in clinopyroxene from the Narce Area, 56. The American Mineralogist, Italy, pp. 959–979.

Izbekov, P.E., Eichelberger, J.C., Ivanov, B.V., 2004. The 1996 Eruption of Karymsky Volcano, Kamchatka: Historical Record of Basaltic Replenishment of an Andesite Reservoir. J. Petrol. 45, 2325–2345. https://doi.org/10.1093/petrology/egh059.

Jicha, B.R., Scholl, D.W., Singer, B.S., Yogodzinski, G.M., Kay, S.M., 2006. Revised age of aleutian island arc formation implies high rate of magma production. Geology 34, 661. https://doi.org/10.1130/g22433.1.

Kahl, M., Chakraborty, S., Costa, F., Pompilio, M., 2011. Dynamic plumbing system beneath volcanoes revealed by kinetic modeling, and the connection to monitoring data: An example from Mt. Etna. Earth Planet. Sci. Lett. 308, 11–22. https://doi.org/10.1016/j.epsl.2011.05.008.

Kahl, M., Chakraborty, S., Costa, F., Pompilio, M., Liuzzo, M., Viccaro, M., 2013. Compositionally zoned crystals and real-time degassing data reveal changes in magma transfer dynamics during the 2006 summit eruptive episodes of Mt. Etna. Bull. Volcanol. 75 https://doi.org/10.1007/s00445-013-0692-7.

Kilgour, G.N., Saunders, K.E., Blundy, J.D., Cashman, K.V., Scott, B.J., Miller, C.A., 2014. Timescales of magmatic processes at Ruapehu Volcano from Diffusion Chronometry and their comparison to monitoring data. J. Volcanol. Geotherm. Res. 288, 62–75. https://doi.org/10.1016/j.jvolgeores.2014.09.010.

King, P.L., Wheeler, V.M., Renggli, C.J., Palm, A.B., Wilson, S.A., Harrison, A.L., Morgan, B., Nekvasil, H., Troitzsch, U., Mernagh, T., Yue, L., Bayon, A., DiFrancesco, N.J., Baile, R., et al., 2018. gas–solid reactions: Theory, experiments and case studies relevant to Earth and planetary processes: High Temperature Gas-Solid Reactions in Earth and Planetary Processes, 1, pp. 1–56. https://doi.org/10.1515/rmg.2018.84.1.

Kirkpatrick, R.J., 1977. Nucleation and growth of plagioclase, Makaopuhi and Alae Lava Lakes, Kilauea Volcano, Hawaii. Geol. Soc. Am. Bull. 88, 78. https://doi.org/10.1130/0016-7606(1977)88<78:nagopm>2.0.co;2.

Larsen, J.F., 2005. Experimental study of plagioclase rim growth around anorthite seed crystals in rhyodacitic melt. Am. Mineral. 90, 417–427. https://doi.org/10.2138/am.2005.1456.

Lasdon, L.S., Fox, R.L., Ratner, M.W., 1974. Nonlinear optimization using the generalized reduced gradient method: Revue française d'automatique, informatique, recherche opérationnelle. Recherche opérationnelle 8, 73–103. https://doi.org/10.1051/ro/197408v300731.

Leake, B.E., 1978. Nomenclature of amphiboles. Bull. Mineral. 101, 453–467. https://doi.org/10.3406/bulmi.1978.7215.

Leonard, G., Cole, J., Nairn, I., Self, S., 2002. Basalt triggering of the c. AD 1305 Kaharoa rhyolite eruption, Tarawera Volcanic Complex, New Zealand. J. Volcanol. Geotherm. Res. 115, 461–486. https://doi.org/10.1016/s0377-0273(01)00326-2.

Loewen, M.W., Izbekov, P., Moshrefzadeh, J., Coombs, M., Larsen, J., Graham, N., Harbin, M., Waythomas, C., Wallace, K., 2019. Petrology of the 2016–2017 eruption of Bogoslof Island, Alaska. Bull. Volcanol. 81 https://doi.org/10.1007/s00445-019-1333-6.

Lopez, T., Clarisse, L., Schwaiger, H., Van Eaton, A., Loewen, M., Fee, D., Lyons, J., Wallace, K., Searcy, C., Wech, A., Haney, M., Schneider, D., Graham, N., 2020. Constraints on eruption processes and event masses for the 2016–2017 eruption of Bogoslof Volcano, Alaska, through evaluation of Iasi Satellite SO2 masses and complementary datasets. Bull. Volcanol. 82 https://doi.org/10.1007/s00445-019-1348-z.

Marsh, B.D., Leitz, R.E., 1979. Geology of Amak Island, Aleutian Islands, Alaska. J. Geol. 87, 715–723. https://doi.org/10.1086/628461.

Martin, V.M., Morgan, D.J., Jerram, D.A., Caddick, M.J., Prior, D.J., Davidson, J.P., 2008. Bang! Month-scale eruption triggering at Santorini volcano. Science 321, 1178. https://doi.org/10.1126/science.1159584.

McCanta, M.C., Rutherford, M.J., Hammer, J.E., 2006. Pre-eruptive and syn-eruptive conditions in the Black Butte, California dacite: Insight into crystallization kinetics in a silicic magma system. J. Volcanol. Geotherm. Res. 160, 263–284. https://doi.org/10.1016/j.jvolgeores.2006.10.004.

Miller, T.P., McGimsey, R., Richter, D., Riehle, J., Nye, C., Yount, M., Dumoulin, J., 1998. Bogoslof. In: Catalog of the Historically Active Volcanoes of Alaska. U.S. Dept. of the Interior, U.S. Geological Survey, Anchorage, AK, AK, pp. 54–57.

Morgan, D., Blake, S., Rogers, N., Devivo, B., Rolandi, G., Macdonald, R., Hawkesworth, C., 2004.. Time scales of crystal residence and magma chamber volume from modeling of diffusion profiles in phenocrysts: Vesuvius, 1944. Earth Planet. Sci. Lett. 222, 933–946. https://doi.org/10.1016/j.epsl.2004.03.030.

Müller, T., Dohmen, R., Becker, H.W., Heege, J.H.T., Chakraborty, S., 2013. Fe–Mg interdiffusion rates in clinopyroxene: experimental data and implications for Fe–Mg exchange geothermometers. Contrib. Mineral. Petrol. 166, 1563–1576. https://doi.org/10.1007/s00410-013-0941-y.

Murphy, M.D., Sparks, R.S.J., Barclay, J., Carroll, M.R., Lejeune, A.-M., Brewer, T.S., Macdonald, R., Black, S., Young, S., 1998. The role of magma mixing in triggering the current eruption at the Soufriere Hills Volcano, Montserrat, West Indies. Geophys. Res. Lett. 25, 3433–3436. https://doi.org/10.1029/98gl00713.

Philpotts, A.R., Ague, J.J., 2009. Principles of igneous and metamorphic petrology: Cambridge. Cambridge University Press.

Putirka, K.D., 2008. 3. thermometers and barometers for volcanic systems. In: Minerals, Inclusions And Volcanic Processes, pp. 61–120. https://doi.org/10.1515/9781501508486-004.

Ruppert, N.A., Lees, J.M., Kozyreva, N.P., 2007. Seismicity, earthquakes and structure along the Alaska-aleutian and Kamchatka-Kurile subduction zones: A Review. In: Volcanism and Subduction: The Kamchatka Region, pp. 129–144. https://doi.org/10.1029/172gm12.

Ruth, D.C., Costa, F., 2021. A petrological and conceptual model of Mayon Volcano (Philippines) as an example of an open-vent volcano. Bull. Volcanol. 83 https://doi.org/10.1007/s00445-021-01486-9.

Ruth, D.C.S., Cottrell, E., Cortes, J.A., Kelley, K.A., Calder, E.S., 2016. From Passive Degassing to Violent Strombolian Eruption: the Case of the 2008 Eruption of Llaima Volcano, Chile. J. Petrol. 57, 1833–1864. https://doi.org/10.1093/petrology/egw063.

Ruth, D.C.S., Costa, F., Maisonneuve, C.B.D., Franco, L., Cortés, J.A., Calder, E.S., 2018. Crystal and melt inclusion timescales reveal the evolution of magma migration before eruption. Nat. Commun. 9 https://doi.org/10.1038/s41467-018-05086-8.

Saunders, K., Blundy, J., Dohmen, R., Cashman, K., 2012a. Linking Petrology and Seismology at an Active Volcano. Science 336, 1023–1027. https://doi.org/10.1126/science.1220066.

Saunders, K., Rinnen, S., Blundy, J., Dohmen, R., Klemme, S., Arlinghaus, H.F., 2012b. TOF-SIMS and electron microprobe investigations of zoned magmatic orthopyroxenes: First results of trace and minor element analysis with implications for diffusion modeling. Am. Mineral. 97, 532–542. https://doi.org/10.2138/am.2012.3893.

Schneider, D.J., Eaton, A.R.V., Wallace, K.L., 2020. Satellite observations of the 2016–2017 eruption of Bogoslof Volcano: aviation and ash fallout hazard implications from a water-rich eruption. Bull. Volcanol. 82 https://doi.org/10.1007/s00445-020-1361-2.

Scholl, D.W., von Huene, R., 2007. Crustal recycling at modern subduction zones applied to the past—issues of growth and preservation of continental basement crust, mantle geochemistry, and supercontinent reconstruction. Geological Society of America Memoirs 9–32. https://doi.org/10.1130/2007.1200(02).

Schwandt, C.S., Cygan, R.T., Westrich, H.R., 1998. Magnesium self-diffusion in orthoenstatite. Contrib. Mineral. Petrol. 130, 390–396. https://doi.org/10.1007/s004100050373.

Shamloo, H.I., Till, C.B., 2019. Decadal transition from quiescence to Supereruption: Petrologic investigation of the Lava Creek Tuff, Yellowstone Caldera, WY. Contrib. Mineral. Petrol. 174 https://doi.org/10.1007/s00410-019-1570-x.

Tepp, G., Dziak, R.P., Haney, M.M., Lyons, J.J., Searcy, C., Matsumoto, H., Haxel, J., 2019. Seismic and hydroacoustic observations of the 2016–17 bogoslof eruption. Bull. Volcanol. 82 https://doi.org/10.1007/s00445-019-1344-3.

Till, C.B., Vazquez, J.A., Boyce, J.W., 2015. Months between rejuvenation and volcanic eruption at Yellowstone caldera, Wyoming. Geology 43, 695–698. https://doi.org/10.1130/g36862.1.

Turner, S.J., Izbekov, P., Langmuir, C., 2013. The Magma Plumbing System of bezymianny volcano: Insights from a 54year time series of trace element whole-rock geochemistry and amphibole compositions. J. Volcanol. Geotherm. Res. 263, 108–121. https://doi.org/10.1016/j.jvolgeores.2012.12.014.

Van Eaton, A.R., Schneider, D.J., Smith, C.M., Haney, M.M., Lyons, J.J., Said, R., Fee, D., Holzworth, R.H., Mastin, L.G., 2020. Did ice-charging generate volcanic lightning during the 2016–2017 eruption of Bogoslof Volcano, Alaska? Bull. Volcanol. 82 https://doi.org/10.1007/s00445-019-1350-5.

Venezky, D.Y., Rutherford, M.J., 1999. Petrology and Fe–Ti Oxide Reequilibration of the 1991 Mount Unzen mixed magma. J. Volcanol. Geotherm. Res. 89, 213–230. https://doi.org/10.1016/s0377-0273(98)00133-4.

Waters, L.E., Andrews, B.J., Lange, R.A., 2015. Rapid crystallization of plagioclase phenocrysts in silicic melts during fluid-saturated ascent: Phase equilibrium and decompression experiments. J. Petrol. 56, 981–1006. https://doi.org/10.1093/petrology/egv025.

Waythomas, C.F., Cameron, C.E., 2018. Historical eruptions and hazards at Bogoslof Volcano. Scientific Investigations Report, Alaska. https://doi.org/10.3133/sir20185085.

Waythomas, C.F., Loewen, M., Wallace, K.L., Cameron, C.E., Larsen, J.F., 2020. Geology and eruptive history of Bogoslof Volcano. Bull. Volcanol. 82 https://doi.org/10.1007/s00445-019-1352-3.

Wech, A., Tepp, G., Lyons, J., Haney, M., 2018. Using Earthquakes, T Waves, and Infrasound to Investigate the Eruption of Bogoslof Volcano, Alaska. Geophys. Res. Lett. 45, 6918–6925. https://doi.org/10.1029/2018gl078457.

Zellmer, G.F., Blake, S., Vance, D., Hawkesworth, C., Turner, S., 1999. Plagioclase residence times at two island arc volcanoes (Kameni Islands, Santorini, and Soufriere, St. Vincent) determined by Sr diffusion systematics. Contrib. Mineral. Petrol. 136, 345–357. https://doi.org/10.1007/s004100050543.